Alma Mater Studiorum - Università di Bologna

Dipartimento di Chimica Industriale “Toso Montanari”

Corso di Laurea Magistrale in

Chimica Industriale

Classe LM-71 - Scienze e Tecnologie della Chimica Industriale

Azoimidazolium molecular rotary motors powered by visible light

Tesi di laurea sperimentale

CANDIDATO

Letizia Pompili

RELATORE

Prof. Massimiliano Curcio

Anno Accademico 2023-2024

Abstract

In Natura, tantissimi sono gli esempi di macchine molecolari che eseguono le più disparate funzioni rendendo possibile la Vita. Alcune di queste sono deputate al movimento: la miosina produce la contrazione muscolare, e trasporta anche molecole all'interno della cellula. Nei batteri, il flagello permette loro di spostarsi nell'ambiente in cui vivono. Tra le nanomacchine più studiate vi è certamente l'ATP sintasi che fornisce energia a qualsiasi processo cellulare rendendo di fatto possibili le funzioni vitali degli organismi viventi. Un sistema basato su legami ad idrogeno autoassemblati su scala nanometrica è il DNA. Esso copia e trasduce il codice genetico nelle proteine.

La loro esistenza è nota da tempo ma negli ultimi anni si è cercato di comprenderne sempre più in dettaglio il meccanismo del loro funzionamento. Negli ultimi venti anni, ispirandosi direttamente alle macchine naturali sono state sviluppate dei sistemi artificiali che seppur lontani dalla complessità di quelli presenti in natura sono abbastanza sofisticati. Come per le macchine molecolari naturali, i movimenti meccanici implicano sostanziali cambiamenti strutturali e ciò può essere ottenuto nei sistemi artificiali solo se almeno uno dei componenti molecolari della macchina è coinvolto in una reazione chimica. Per farla avvenire è necessario fornire dell'energia al sistema che può essere di tipo chimico, elettrochimico o luminoso.

Ad oggi, le macchine molecolari artificiali possono essere divise in interruttori molecolari e motori molecolari. Nell'interruttore, il cambiamento nelle posizioni relative dei componenti, influenza un sistema in funzione dello stato dell'interruttore. Quando un interruttore viene riportato al suo stato originale, qualsiasi lavoro meccanico eseguito verrà annullato. Al contrario, il lavoro svolto dal motore molecolare quando torna al suo stato originale alla fine del ciclo, non viene annullato.

In questo progetto di tesi, si è voluto sintetizzare e caratterizzare fotochimicamente motori molecolari foto attivati a base di azoimidazolio. I principali vantaggi di utilizzare la luce è che è una fonte energetica accessibile ed intrinsecamente rinnovabile e la reazione che avviene è reversibile e pulita, quindi senza la formazione di prodotti di scarto.

Lo scopo di questo lavoro è proporre una classe differente di motori molecolari foto attivati con l'obiettivo di superare i limiti delle principali classi ad oggi studiate e conosciute. Si è realizzata una sintesi semplice, con pochi step di reazione e a partire da alcuni reagenti commercialmente disponibili. Per applicazioni in ambito biologico è importante che il motore molecolare isomerizzi in luce visibile e si sciolga in acqua. Dopo aver realizzato il primo prototipo di motore molecolare che isomerizza correttamente nella regione dell'ultravioletto, si è cercato di trovare delle strategie semplici per ottenere un composto che risponda a questo scopo. Attraverso la sostituzione con un sostituente elettron-donatore sull'anello aromatico dell'unità diazenica, si è osservato effettivamente uno spostamento del massimo di assorbimento verso la regione del visibile. Inoltre, per consentire lo scioglimento in acqua di questa classe di composti, è stata messa a punto una strategia efficiente basata sullo scambio del controione originale PF_6^- con uno ione Cl^- mediante una resina a scambio ionico.

1. INTRODUCTION

1.1 Nanoscale directional motion control

In the last 30 years chemists worked to improve the control on molecular motion by taking inspiration from biological systems, which exploit biomolecular machines for muscle contraction, motility, cellular cargo transportation, and ATP fuel production. Starting from early theoretical studies, over the years very complex systems have been developed thanks to a deep insight in the principles governing controlled motion at the molecular scale.

A peculiar type of motion undertaken by molecular machines involves the rotation about a specific axle. Such nanodevices are categorized into molecular switches, rotors, and motors, and comprise a rotating unit (rotator) and a stationary part (stator) which are interconnected by an axle usually lying along a bond.

In a molecular switch subjected to an appropriate external stimulus, the rotator unit can reversibly change its position between two or more stable states, while a molecular rotor performs continuous free rotation at room temperature. Nonetheless, in both cases the rotation process is nondirectional, and it can only be controlled in terms of rotation rate as a function of the operational temperature.

In contrast, molecular machines in which the rotation achieves a net directionality (clockwise or counter-clockwise), are labelled as *molecular motors*. The directional bias is conferred by the combination of two or more stereogenic elements, usually consisting in axial chirality coupled to a covalent chiral auxiliary located in the close vicinity of the motor axle. This combination creates a diastereomeric relationship between the forward and backward rotation, overall favoring one with respect to the other.

Besides being directional, the movement undertaken by molecular machines upon provision of external stimuli can be further divided into stepwise or autonomous. In the first case, a single stimulus is not sufficient to induce a complete rotation and only promotes part of it (step). For such reason, multiple sequential operator-bound stimuli should be provided to promote the full directional cycle. On the other hand, autonomous motors are able to constantly carry on full directionally biased cycles as long as the appropriate energy input is provided, without any need for external intervention (operator-independent).

Precise control of long-range motion at the molecular scale holds great potential for the development of applications in energy storage and bionanotechnology. A variety of potential applications is now being considered in areas ranging from catalysis and self-assembly to molecular electronics and responsive materials.

1.2 Biological molecular motors

In all living organisms, vital roles are carried out by molecular motors, proteins or assemblies thereof that continuously and autonomously convert the energy coming from an external source into mechanical or chemical work while performing a directional motion of the components, as it happens in macroscopic engines. In doing so, these chemical systems are set in non-equilibrium states sustained by continuous dissipation of energy. Some of the most important and extensively studied motor proteins are those of the myosin and kinesin families, ATP synthase, and bacterial flagellar motor. Dynein and kinesin protein assemblies are examples of linear motors able to

directionally transport cargoes by “walking” on the surface of microtubules. Myosins on the other hand are able to move along actin filaments to induce muscle extension and contraction. All these protein motors consume chemical energy derived from the hydrolysis of adenosine triphosphate (ATP) to carry out mechanical work.

However, biological motors are not limited to linear movements and encompass also rotary motion. Examples of biological rotary motorsare bacterial flagella and ATP Synthase.

Flagella are cellular appendages that protrude from the membrane to enable motility. Bacterial flagella are the most widely studied motility units and are responsible for bacterial swimming and swarming motions, thanks to an electrochemical ion motive force arising from the transit of ions across the cellular membrane. Structurally, flagella can be divided in three main domains. The filament is the outermost component, it consists of thousands flagellin protein units supramolecularly arranged in an helical shape that extends for several cell lengths in the outer environment. At its base, the filament is linked to the intramembrane motor-containing basal body by a flexible module named hook, which acts as a universal joint to transfer the torque inferred by the rotary motor.

The key mechanical unit, the flagellar rotary motor, is built by about 20 proteins and spans across the outer membrane until the inner membrane, into the cytoplasm. Similar to all rotary motors, its structural constituents are the rotor and the stators.

The rotor is made of four concentric protein rings that are connected by a rod in their center. The stators are located around the periphery of the rotor, forming a larger concentric protein ring outside the MS-ring. It can accommodate 8–12 stator complexes, each of which is made up of 4 MotA and 2 MotB proteins. MotA has a cytoplasmic domain interacting with the rotor to generate torque while MotB has a cytoplasmic domain and a linker domain that anchors the stator complex to the peptidoglycan cell wall. On each stator complex lie two ion channels that allow the passage of protons from the periplasm to the cytoplasm of the cell. The torque is generated between the C-terminal domain of the rotor protein FliG and the cytoplasmic domain of the stator protein MotA. The proton flux coordinates a conformational change in MotA, to drive the rotation by direct interaction with FliG.

Distinct from most linear molecular motors, the bacterial flagellum is powered by the free energy released from the flow of ions down an electrochemical gradient across the cytoplasmic membrane into the cell (protonomotive force).

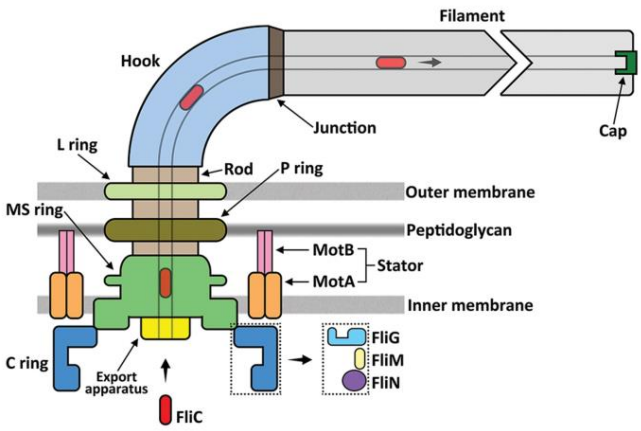

Figure 1.1. Schematic representation of the major structural components of the bacterial flagellum.

Another important biological rotary motor is ATP synthase, a very sophisticated biological molecular machine and one of the most ubiquitous and abundant proteins on Earth. Its function is to produce ATP, and this process is powered by the flow of hydrogen ions along the gradient of electrochemical potential of protons across membranes. This potential is built by the electron-transfer chains of respiration or photosynthesis, which pump protons against a concentration gradient. ATP supports nearly all the cellular activities that require energy. For this reason, ATP synthesis is the most prevalent chemical reaction in the biological world. ATP synthase is a large protein complex of two motors, the ATP-driven F1 motor and the proton-driven Fo motor, connected by a common rotary shaft and having opposite direction of rotation. When the electrochemical potential difference of H^+ between the two phases (when two aqueous phases are separated by a membrane) is large, downhill proton flow through Fo causes rotation of the Fo rotor and, hence, rotation of the γε-subunits of F1. The rotary motion of γ alternates the structure of the β-subunit so that ATP is synthesized.

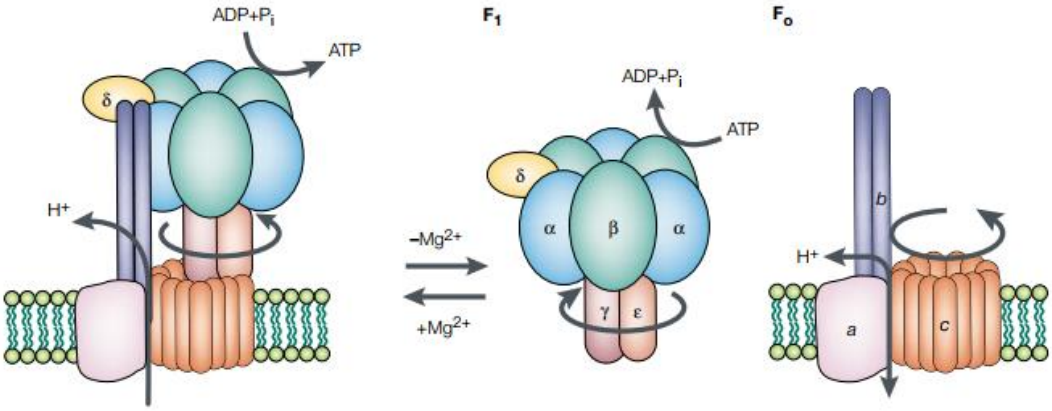

Figure 1.2. Schematic structure of ATP Synthase.

1.3 Artificial molecular machines

In general terms, a molecular machine is defined as a molecule, or ensemble thereof, able to carry out a mechanical movement by displacement of a sub-component upon provision of an external stimulus. More in detail, these nanoscale devices are further classified into switches and motors. In the case of a switch, the change in the relative position of the components influences a system as a function of the state of the switch; however, when a switch is reverted to its original state any mechanical work performed will be undone. In contrast, molecular motors operate along a closed reaction network in a directional fashion such as that when the motor completes a full cycle and returns to its original state the work performed is not undone. Importantly, in contrast to the macroscopic world molecular machines operate in conditions where gravity and inertia are irrelevant and viscous forces and Brownian motion are predominant. These thermal fluctuations highly complicate the execution of controlled precision movements typical of machine-like operation. A careful molecular design making use of a judicious coupling of structures able to

accurately respond to external stimuli is therefore a strict requirement to operate in this environment.

Directly inspired by nature, the ultimate goal about chemically driven molecular machines is to develop controlled, continuous and autonomous motion. Nature uses molecular switches and motors to control molecular functions by altering the properties of a system in response to an external stimulus. Movements are executed as a consequence of the conversion of chemical energy into mechanical energy. Despite the significative fundamental advancements made in the field of artificial molecular machines over the last two decades, in which the design, mechanism of function and exploratory applications were proposed, major challenges remain to be addressed.

Starting from simple components of artificial molecular machines, common types of mechanical movements can be identified:

a) Rotation around single bonds and in sandwich-like metallocenes;

b) Bending due to *cis-trans* isomerization of alkenes and azobenzenes;

c) Translational motion of a ring between two binding sites along the dumbbell-like rotaxane axis;

d) Relative rotation of the interlocked rings in a catenane.

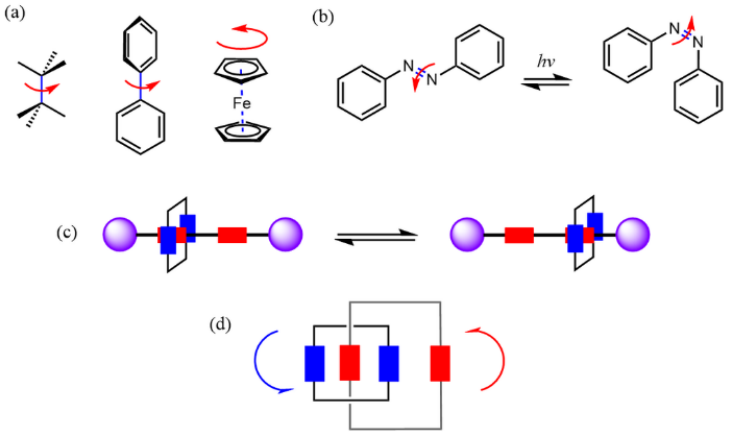

Figure 1.**3.** Examples of mechanical movements.

In general, to operate continuously a motor (macroscopic or microscopic) must go through a closed sequence of transformations which can be repeated indefinitely. Additionally, a careful molecular design is required to achieve unidirectional motion. One strategy can be the introduction of a chiral group in the close vicinity of the rotation axle of a rotor coupled to a chemical transformation to power the rotation. Another useful approach is the use of asymmetric catalysis. Although biological molecular machines use chemical catalysis for their majority of the autonomous processes, only fully functional catalytic rotary motors exist. The other important goal is to minimize the number of reaction steps required to achieve full rotation. For this, researchers have developed transition-metal-catalyzed motor and redox electrochemically driven motor. In contrast, light-driven molecular motors based on overcrowded alkenes are so far rather unique as they undergo, upon sustained irradiation, continuous rotation.

Current challenges in the field of artificial molecular machines include the implementation of the mechanical motion along extended distances, to compounds in the solid state and in biocompatible aqueous media to develop potential biomedical applications.

1.4 Chemically driven molecular motors

Now we'll discuss systems which use chemical interactions such as hydrogen bonding, pH response, metal coordination, conformational change (rotation) due to bond formation and cleavage in dynamic systems, to allow molecular motion. Various types of molecular switches can be categorized based upon conformational changes, through modulation of hydrogen-bonding; a solvent-assisted conformational control; pH-responsive switching in biphenyl; and through ion binding.

1.4.1 Conformational Switching Controlled by Intra/Intermolecular Interactions

In this type of motors the rotation is induced chemically. Over the past decades, hydrogen bonds have became most important in the design of artificial molecular systems. Scientists have developed several molecular machines that exhibit rotation upon manipulation of this weak interaction. For these systems they were inspired from Nature where there are several examples of brilliant use of this interactions. Various nanoscale self-assembled H-bond-based systems carry out essential functions for life. The most indicative is DNA helices which are controlled by the presence of multiple hydrogen bonds between Watson–Crick base pairs.

An example of a carefully-designed molecular switch is provided by *Rac*-**1a**, an axially chiral diacid switch from Shimizu and co-workers. In these system, the precise control of hydrogen bonding is used for their conformational changes.

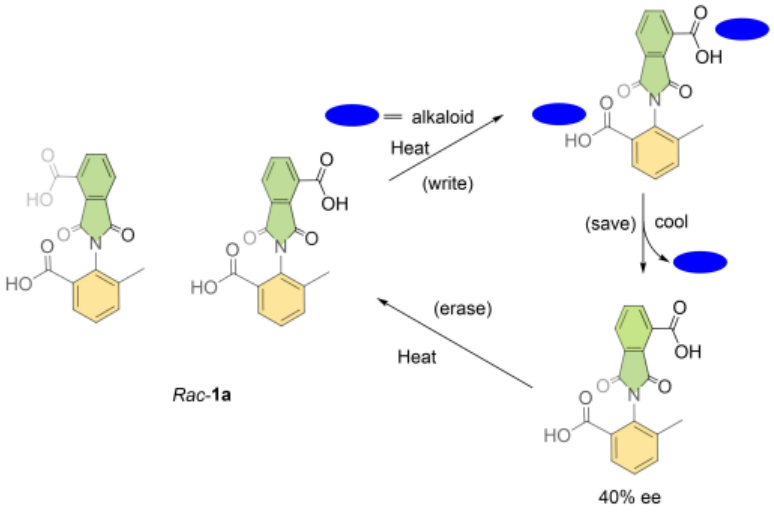

Figure 1.4. Molecular switch *Rac*-**1a** regulated by intermolecular H-bonds.

1.4.2 H-Induced Molecular Switches

The vast majority of biological systems exploit the phenomenon of pH-Induced molecular conformational changes and inspired extensive research. An excellent example of a pH-responsive switch was developed by Yoshizawa and co-workers. With the addition of a base, a selective *cis*–

trans isomerization through rotation around an aryl–aryl bond was induced. The starting compound is a *trans*-anthracene trimer. A base (NaOH) deprotonates one of the hydroxyl groups, triggering the selective isomerization of the *trans*-anthracene trimer to its *cis* isomer, through a 180° rotation around the single bond.

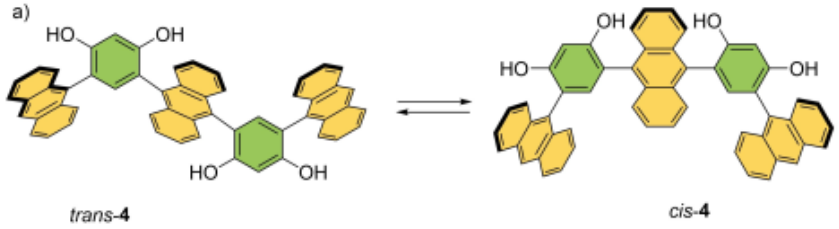

Figure 1.5. Base-controlled switching of molecular conformation in an anthracene trimer.

1.4.3 Metal-Ion-Coordination-Based Molecular Switches Based on Single-Bond Rotation

In this class of molecular machines, rotary motion around single bonds is caused by metal coordination. Coordination complexes have several advantages that can be exploited. In a supramolecular system, metal coordination needs to drive molecular extension and contraction motion via multiple C_{aryl}–C_{aryl} bond rotations. Through complexation, the structure of the molecule changes with the consecutive changes in the conformation.

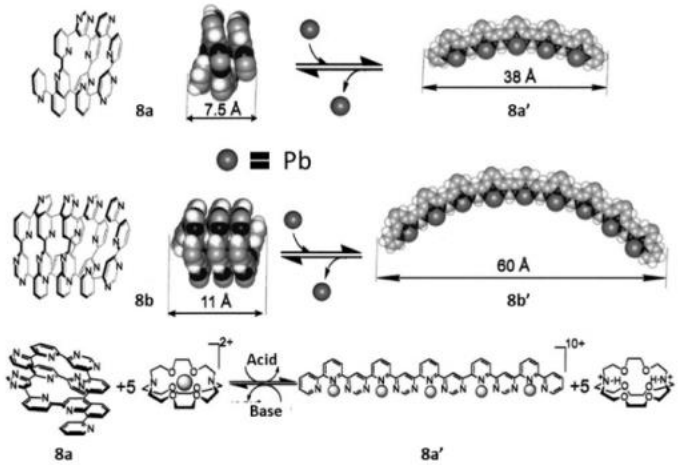

Figure 1.6. Molecular strands switchable between the extended and contracted forms.

1.5 Electrochemically driven molecular motors

Electric powered molecular motors are powered by redox cycles through the flow of electrons. An example of electric molecular motor is based on a [3]catenane, in which two cyclobis(paraquat-p-phenylene) ($CBPQT^{4+}$) rings are powered by electricity in solution to circumrotate unidirectionally around a 50-membered loop. For simplicity, we will refer to the $CBPQT^{4+}$ rings and the 50-membered loop as A and B. A bis(4-methylenephenyl)methane (BPM) unit separates two viologen (V^{2+}) units, which on reduction access their $V^{+\bullet}$, to serve as recognition sites for reduced CBPQT2($^{+\bullet}$) rings. The rest of the loop is composed of an oligomethylene chain and one oxygen atom, intercepted along its length by an isopropylphenylene (IPP) steric barrier, a triazole (T) ring, which is generated during the

final ring closure of the loop to give the [3]catenane, and a 2,6-dimethylpyridinium (PY^+). The presence on the cycle of units that create steric hindrance causes the rings to move towards a preferential direction, the clockwise rotation is faster than the counterclockwise one and this will mean that the rotation will mainly be towards a preferential direction.

Starting from the bipyridine unit (V^{2+}) reduction provides a radical cation, which is a stable species with 13 π electrons, while further reduction leads to a neutral species (14 π electrons). As the charge on the V^{2+} unit gets reduced, the $CBPQT^{4+}$ ring begins to associate thanks the π stacking interactions of the bipyridine rings. Conversely, when the bipyridine units are oxidized the rings move to the next station. Although the two $CBPQT^{4+}$ rings are identical, so after just one reduction / oxidation cycle an equivalent system to the initial one is obtained, to have ring A in the original position a second cycle must be carried out.

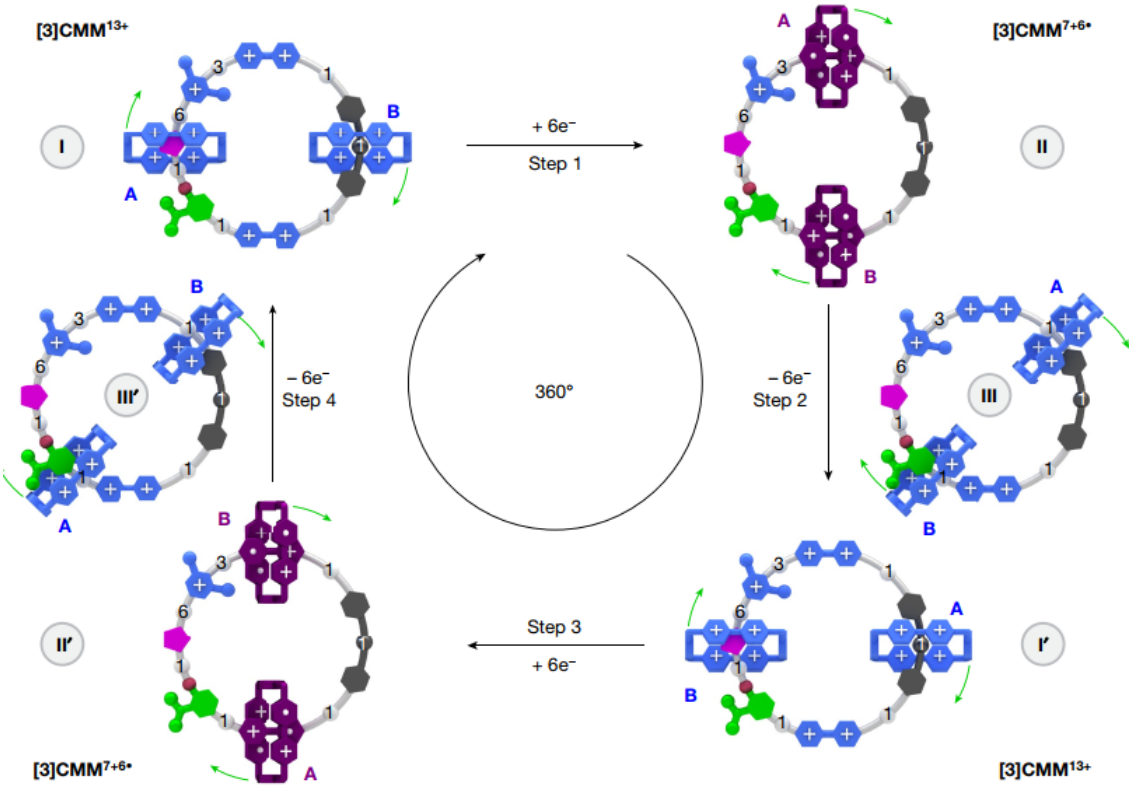

Figure 1.7. [3]catenane molecular motor powered by electrons.

1.6 Photoactivated artificial molecular motors

Molecular motors driven by chemical reactions work well but have the major limitation of waste accumulation; this accumulation resulting from a high number of cycles changes the chemical environment, compromising its functioning. Molecular motors built in flow partially resolve this problem. As regards electric motors, the technology to use these systems is well implemented but such molecules were proven to undergo decomposition after a few work cycles. Compared to chemical and electrochemical stimuli, the use of light as an energy source is highly advantageous because light widely accessible and intrinsically renewable, provides potentially clean reactions, and has high spatiotemporal control. However, these systems require a specific molecular design that

involves a clever combination of photochemical and thermal rearrangement processes. All the motors work by repeating and reversible cycles, so high efficiencies and fatigue-resistant reactions are required. For this reason, only a few types of photochemical reactions have been employed, like photoinduced electron transfer and photoisomerization processes. Focusing on the latter, the main classes of molecules used in photoisomerization reactions are stilbenes, imines and azobenzenes.
Three classes of light-driven molecular motors have been reported to date, and all of them display covalent molecular structures that exhibit rotary motion of one subunit with respect to another. In general, light-driven artificial molecular motors work by coupling a photoinduced reaction with a thermal rearrangement process. Since each of these processes typically interconverts two states, the result is a four-membered closed reaction network. Indeed, this is not a sufficient condition to obtain a motor; the other characteristic is the unidirectionality. The nanoscopic world requires the use of an energy source to bias Brownian motion and render the movement in a given direction more favored than those in other directions. This because thermal energy results in an endless "jiggling" of the atoms which disrupts any directionality.
An important aspect in photochemical reactions is that the composition (the product/reactant concentration ratio) at the photostationary state (PSS) is determined by the photoreaction quantum yields governed solely by the profile of the excited-state potential energy surface and the molar absorption coefficients. Thus, these reactions are not bound to the constraints of microscopic reversibility, which instead regulate thermally activated processes in the electronic ground state.

1.6.1 Overcrowded alkenes

Such compounds can be categorized in two distinct families based on their substitution patterns, such as a stilbene core or a sulfur-based hemithioindigo heterocycle.

Feringa motors

The first photochemical *cis–trans* isomerization around a central carbon–carbon double bond was achieved in stilbene. However, due to the symmetry of stilbene, there can not be any directional preference in the isomerization process. In 1977, the introduction of steric bulk around the double bond gave rise to helical chirality. This work formed the basis for the design and synthesis of the first molecule capable of undergoing unidirectional 360° rotation about a double bond. In 1999, Feringa and co-workers synthesized an overcrowded alkene compound having two identical halves on each side of the double bond (the rotary axle). Each half further presented two stereogenic methyl substituents which dictate the helical chirality and hence the direction of rotation. This structure became later known as the first-generation molecular rotary motor. Subsequent developments led to the second-generation, in which the presence of only one stereogenic center is sufficient to induce unidirectional rotation. A pseudo-asymmetric center was also adopted to access unidirectional rotary motion around both axles and became the distinct characteristic of the third-generation of rotary motors. Finally, in fourth-generation motors, the preferential direction of rotation is enforced by a chiral guest molecule that can bind non-covalently to a light-activated switch. In other words, it is a supramolecular transfer of chirality from the optically active guest that induces the unidirectional rotation around the double bond of the photoswitchable receptor is induced from the optically active guest which acts like a supramolecular transfer of chirality. Nonetheless, despite their

extensive development these systems still present a number of limitations, including a time-inefficient and complex synthesis and a pronounced hydrophobicity that hinders any operation in aqueous media.

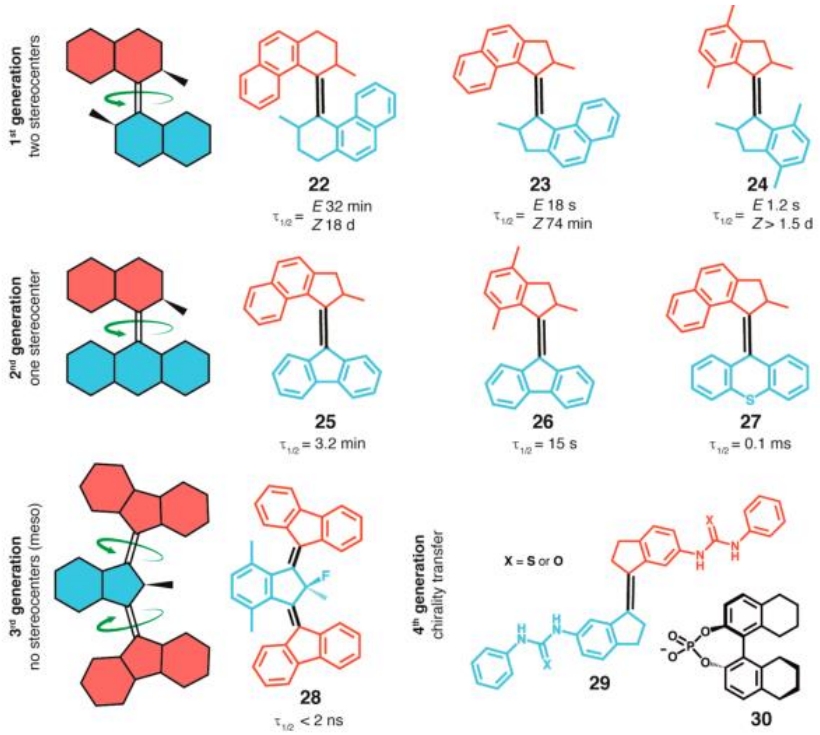

Figure 1.8. Different generations of light-activated rotary motors of the overcrowded alkene family.

Dube motors

Dube and co-workers designed a hemithioindigo motor with an atropisomeric aryl unit. The interest in using this heterocycle is motivated by its absorption in the visible range and the fast rates of rotation achieved. Notably, the torque imparted by the motor through the tether has a catalytic effect on the epimerization of the axial chirality in a preferred direction, however, thermodynamic equilibrium between the two atropisomers cannot be maintained under operation. Overall, these motors have high efficiency but maintain a complex synthesis and a poorly implementable heteroaryl structure.

1.6.2 Imines

These systems involve an isomerization process of the C=N double bond which, coupled with inversion of planar chirality, results in a four-membered closed reaction cycle. Light irradiation leads to a non-equilibrium *Z*/*E* mixture of isomers attained by out-of-plane rotation about the C=N double bond. The difference with respect to overcrowded alkenes, is that two independent reaction pathways could be undertaken, namely rotation or inversion at the N atom.

1.7 Applications of molecular motors

Making molecular machines that can be useful in the macroscopic world is a long-term goal of nanoscience. Today, all the molecular machines which exist are inspired by nature. An applicative area towards which molecular motors present high potential is that of smart materials. Relevant examples include mechanically active gels based on chemically crosslinked polymer-motor conjugate system. Its entangled topology made by polymer chains can be affected by the motor directional rotation upon irradiation, causing a macroscopically observable shrinking.

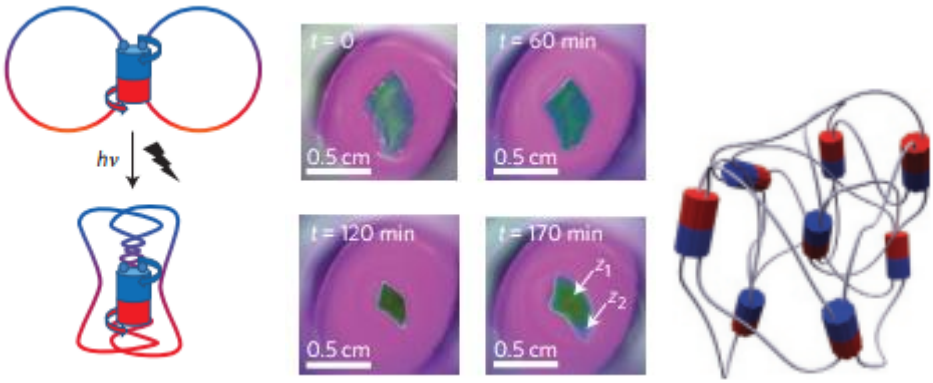

Figure 1.9. Light-responsive smart materials exploiting molecular rotary motors.

Another potential applicative sector is that of photopharmacology. The most developed approach is photodynamic therapy, where a photosensitizing dye molecule is administered to patients. Absorption of light by the dye results in the formation of a dye excited state, which in turn forms reactive intermediates such as reactive oxygen species (ROS). The other two approaches are based on the photochemistry of photopharmacological agents that can be irreversible or reversible, dependent on the molecule in question. The most well-known example of the former is photodecaging, in which a photoactive protecting group is added to a biological ligand to mask key pharmacophoric features of the ligand and deactivate its target-based activity. Irradiation results in photochemical cleavage of the group and release of the active biological agent. The last approach uses a reversible photopharmacological agent that operates through a molecular photoswitch enbedded into its structure. By coupling a photoswitch component to a biologically active ligand, light can be used to switch the ligand between the two states. Assuming the two different structural states have dramatically different binding affinity to the target, light can switch target-based activity on and off. The majority of reversible photopharmacology approaches use azo aromatics such as azobenzene which can be incorporated in different ways. Its remarkable stability and efficient photoswitching allow operation with low-intensity light repeated switching over multiple cycles.

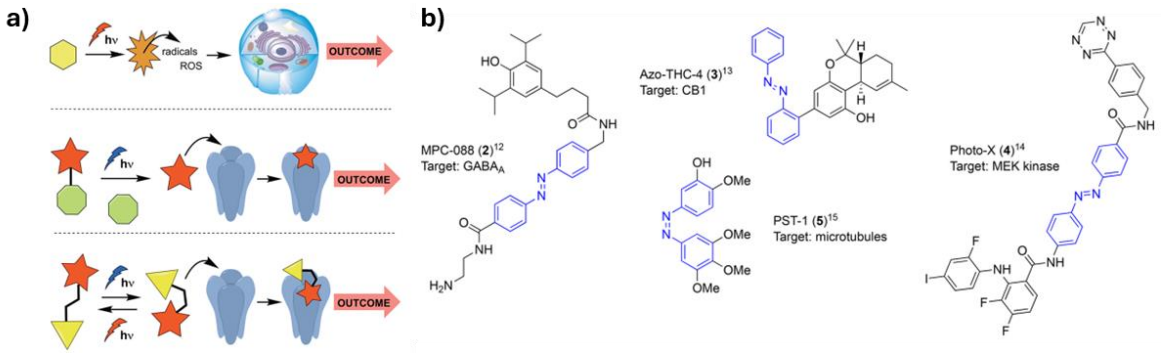

Figure 1.10. *a)* Light-dependent pharmacological approaches: (top) photodynamic therapy (ROS = reactive oxygen species), (middle) irreversible photopharmacology (photodecaging), (bottom) reversible photopharmacology with a ligand that is active only in one structural state; *b)* Azobenzene-derived photopharmacology agents.

1.8 Diazene molecular switches

Azobenzene is a diazene derivative where both hydrogens are replaced by phenyl groups and can exist in either the stable *trans* or the metastable *cis* configurations. The *trans* → *cis* isomerization occurs following irradiation with UV-visible light, mechanical stress or electrostatic stimulation, while *cis* → *trans* isomerization can be light-driven or occur spontaneously in the dark. The formation of compact *cis* form is accompanied by the change of many physical properties such as dipole moment, dielectric constant and refractive index. Interestingly, azobenzene is able to isomerize under strong constraints, for example in solid matrices. All these properties make azobenzene and its derivatives good candidates as integrated photoresponsive units in a variety of polymers, surface-modified materials, protein probes, molecular machines, holographic recording devices and metal ion chelators.

1.9 Aim of the thesis work

In the present study, a cationic diazene photoswitch with an imidazole-based heterocyclic core was developed. Analogously to azobenzene, such photochromic compound is able to interconvert between linear *E* and bent *Z* isomers upon light irradiation. Additionally, here two diastereomeric *Z*-isomers are produced by combining a non-symmetric substitution pattern at the endocyclic nitrogen atoms, the photogenerated axial chirality of the *Z*-diazene and a fixed stereogenic center. Through the combination of the different photoreactivity of the diastereomers and their interconversion by rotation about a single C–N bond, a net directional travel across a closed reaction upon continuous illumination was achieved. To further evaluate the potential of this class of compounds, the influence of the substitution pattern at the arylazo group on the absorption properties as well as the effect of the counterion were carefully assessed.

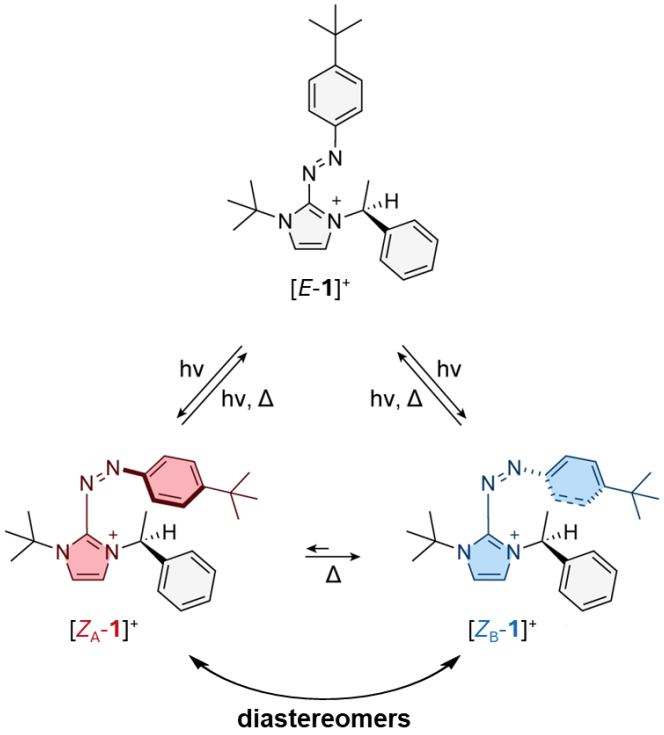

Figure 1.11. Structure and reaction network of operation of one of the molecular rotary motors developed in this thesis work.

2. EXPERIMENTAL SECTION

2.1 Materials

All the reagents and solvents used have been purchased from Sigma Aldrich and Fluorochem, without further purification.

2.2 Instruments and methods

2.2.1 Nuclear magnetic resonance spectroscopy

The ^{1}H, ^{19}F and ^{13}C NMR spectra were recorded at 298 K in deuterated solvents (from Cambridge Isotope Laboratories, Inc.) by using either a Varian DD3 500 MHz spectrometer or a Varian Mercury 400 MHz spectrometer with the deuterated solvent as a lock and the residual solvent as the internal standard. All chemical shifts (δ) are quoted in ppm and all coupling constants (*J*) are expressed in Hertz (Hz).

2.2.2 UV-visible spectroscopy

Absorption spectra were recorded using a Perkin Elmer Lambda750 double beam spectrophotometer on air-equilibrated $CHCl_3$ (HPLC grade) or Milli-Q water solutions at RT. In the case of fast process experiments, a diode array spectrophotometer (Avantes) coupled to a Hg lamp was used. The solutions were examined in spectrofluorimetric quartz cuvettes of 1 cm optical path length.

2.2.3 Photochemical reactions

Irradiation experiments were performed on air equilibrated solutions, thoroughly stirred, using a medium pressure Hg lamp (200 W) at room temperature. The Hg lamp was also coupled with a diode array spectrophotometer Avantes StarLine AvaSpec-ULS2048CL-EVO-RS to collect absorption spectra with high rates under continuous irradiation. The diode array spectrophotometer was equipped with an optical fibre which enables the fast acquisition of absorption spectra (ms) and concomitant in situ irradiation. The desired wavelength of irradiation was selected using an appropriate interference filter. The incident photon flux of the irradiation lamp was determined to be 4.4×10^{-9} Einstein s^{-1}, 2.8×10^{-9} Einstein s^{-1} and 4.3×10^{-9} Einstein s^{-1} respectively at 365 nm, 405 nm and 436 nm, using the 4,4′-dimethylazobenzene actinometer. The absorption spectra of the unknown *Z*-isomers were extrapolated mathematically, according to the method reported by Fischer in 1967. The photoisomerization quantum yields ($\Phi_{E\rightarrow Z}$) were determined from the disappearance of the π-π* band of the diazene unit by fitting the initial part of the global photokinetic taking into account just low conversion percentages (<10%). This choice was required by the need to consider negligible the quantum yield of the photochemical back-isomerization processes ($\Phi_{Z\rightarrow E}$), since only mathematically extrapolated absorption spectra of pure *Z*-isomers could be obtained for the investigated molecules. The fraction of light transmitted at the irradiation wavelength was taken into account in the calculation of the quantum yields. The fitting was performed using the software Berkeley Madonna. The rate constants for thermal back-isomerization reactions were obtained by

fitting the back-isomerization spectral data at the maximum wavelength against time using a first-order kinetics (exponential) model in OriginPro 2021.

2.3 Results and discussion

The target compounds were synthesized adopting the general approach reported in **Scheme 2.1.** The corresponding minimalistic synthetic pathway was devised to obtain the molecular rotary motors through time-effective, high yielding and readily scalable protocols. Overall, the procedures could be reduced to a convenient three-step synthesis due to the commercial availability of *N*-*tert*-butylimidazole and of the chiral benzylic bromide, but for the sake of completeness each individual step was conducted during this experimental work and will be discussed in the following paragraph.

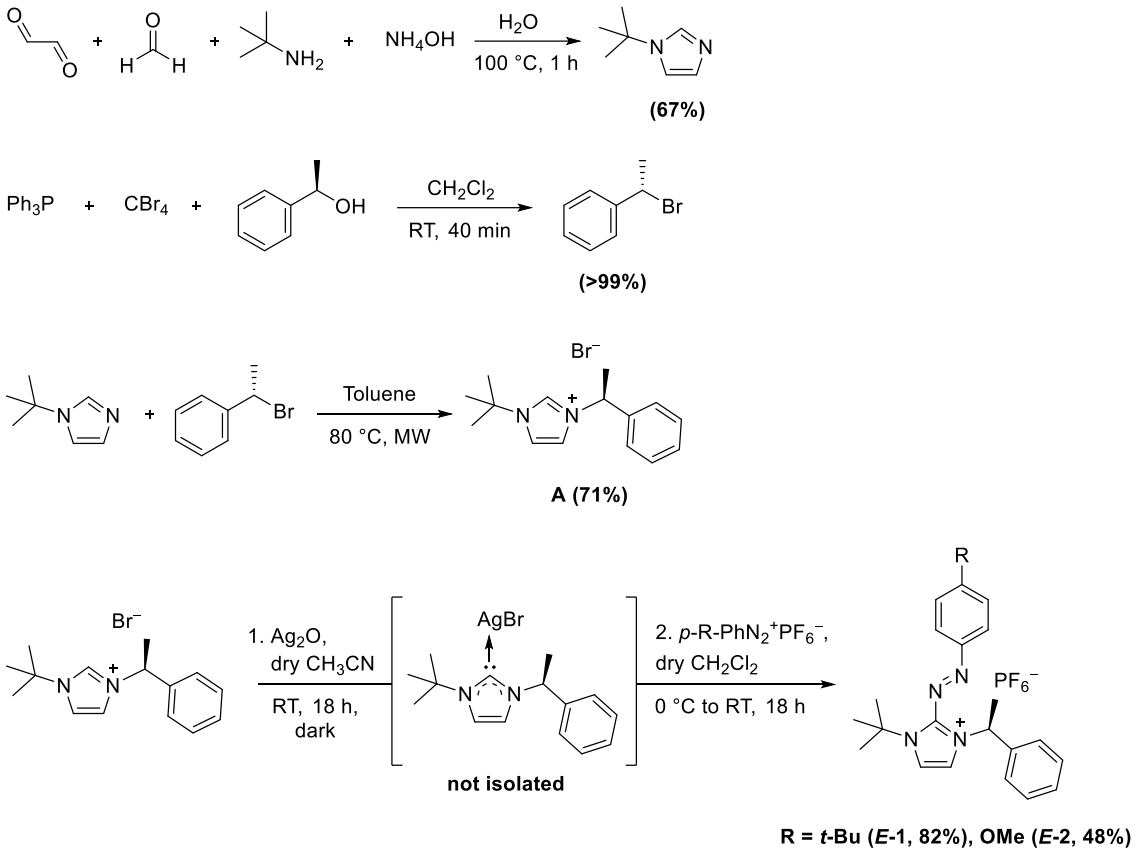

Scheme 2.1. Synthetic pathway to the targeted molecular motors.

N-*tert*-butylimidazole was synthesized by dropwise addition over time of equimolar quantities of i) *tert*-butylamine and ammonium acetate, and ii) glyoxal and formaldehyde to refluxing water. Extraction with DCM provided a crude dark oil which was purified through silica filtration to obtain the orange oil product, whose identity was confirmed through ^{1}H NMR analysis (**Figure 2.2**). The product ^{1}H NMR spectrum shows a singlet at 1.51 ppm related to the *tert*-butyl group, together with two aromatic resonances at 7.00 ppm and 7.01 ppm for the backbone hydrogen and a deshielded N=CH–N resonance at 7.56 ppm.

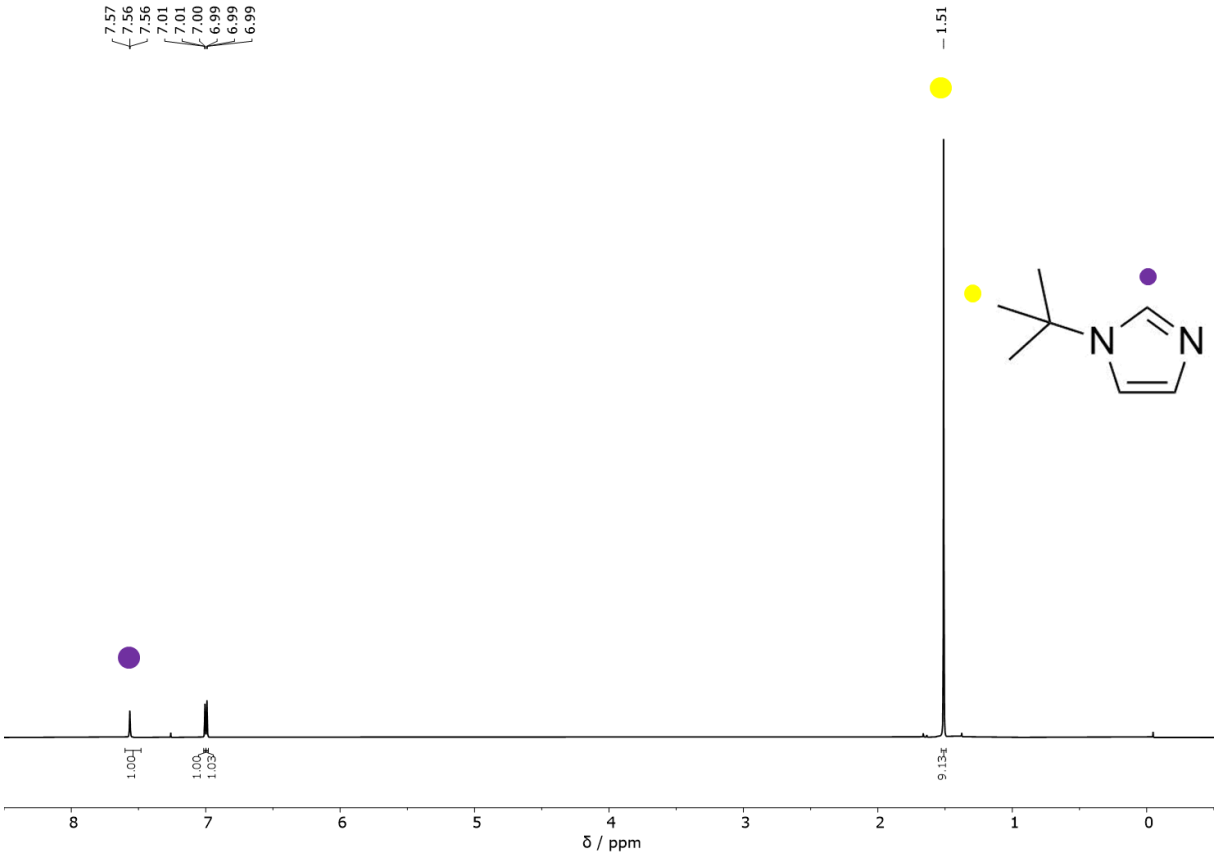

Figure 2.2 ^{1}H NMR spectrum of *N*-*tert*-butylimidazole; $CDCl_3$, 500 MHz, 298K.

To access the key chiral imidazolium intermediate **A**, *N*-*tert*-butylimidazole must be further functionalized with a chiral alkyl group, and thus required the preparation of the chiral benzyl bromide starting from the corresponding commercially available and inexpensive alcohol. The latter was therefore reacted with triphenylphosphine in CBr_4 according to classic Appel reaction conditions to obtain the desired chiral benzylic bromide product. ^{1}H NMR characterization of the product shows a resonance pattern consistent with the product structure and displaying the CH quartet at 5.22 ppm, the methyl doublet at 2.05 ppm and the phenyl ring resonances in the aromatic region (**Figure 2.3**).

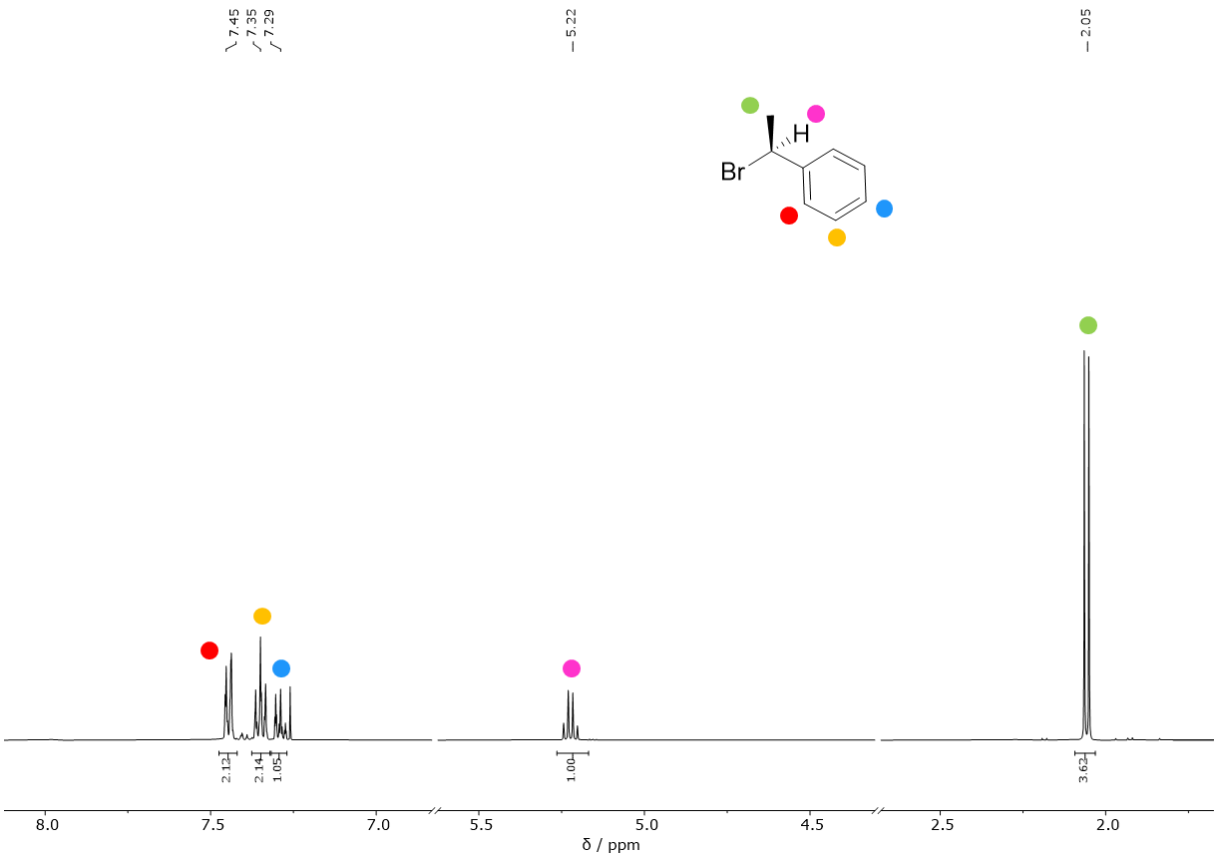

Figure 2.3. ^{1}H NMR spectra of the chiral bromide product; $CDCl_3$, 500 MHz, 298K.

The reaction between *N*-*tert*-butylimidazole and the chiral benzylic bromide was carried out at 80 °C in a microwave reactor using toluene as the solvent. The efficient heating of the microwave reactor allowed a clean and complete reaction to be achieved in 2 h. Conveniently, the ionic nature of the product makes it insoluble in apolar solvents like toluene and thus easily separated from residual starting materials and potential impurities. The ^{1}H NMR spectrum of the solid precipitate displays several resonances supporting the formation of the desired product **A** (**Figure 2.4**). The resonances characteristic of the chiral fragment are maintained, with a considerable deshielding (Δδ = 1.1 ppm with respect to the benzylic bromide) for the quartet related to the benzylic CH, consistent with its substitution with a cationic heterocycle. The *tert*-butylimidazole peaks are also present, with deshielded resonances for the tert-butyl substituent and the backbone protons. Final evidence lies in the large downfield shift undertaken by the N=CH–N proton, whose singlet moved from 7.56 ppm to 10.82 ppm as a consequence of the synthesis of the cationic imidazolium ring.

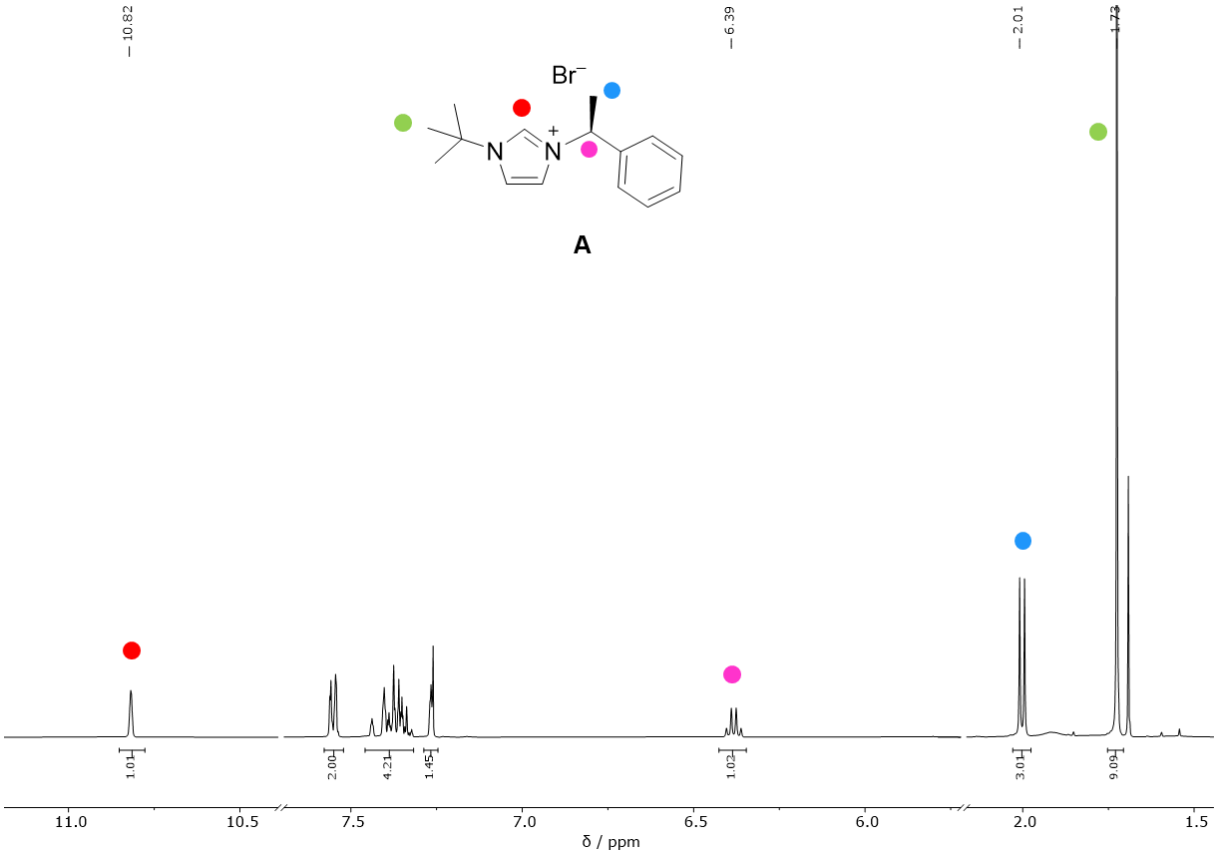

Figure 2.4. ^{1}H NMR spectrum of **A**; $CDCl_3$, 500 MHz, 298K.

Imidazolium bromide **A** was reacted with silver oxide in dry acetonitrile to access the corresponding silver-*N*-Heterocyclic Carbene (NHC) complex. The solution containing the silver-NHC complex was filtered to remove excess silver oxide and potentially reduced colloidal silver, and added to a dichloromethane solution containing an appropriate diazonium hexafluorophosphate salt (either *p*-*tert*-butyl or *p*-methoxy substituted). The latter was independently synthesized by reacting the corresponding aniline with sodium nitrite in water in the presence of hexafluorophosphoric acid.

Combining the nucleophilicity of the carbene ligand, the electrophilicity of the diazonium cation and the poor solubility of silver bromide, the reaction efficiently leads to the formation of the arylazoimidazolium hexafluorophosphate motors with the removal of silver bromide as a colorless precipitate. Pure products *E*-**1** and *E*-**2** were obtained as crystalline orange solids upon purification by column chromatography and gel permeation chromatography. The ^{1}H NMR spectra of both diazene products display sets of resonances consistent with the formation of the desired structures. In the case of *E*-**1** (**Figure 2.5**) it is possible to identify the characteristic peaks of the chiral benzylic fragment as the CH quartet at 6.26 ppm and the methyl doublet at 1.93 ppm; the *N*-*tert*-butyl fragment resonance lies deshielded at 1.85 ppm. The resonances of the aryl group are also consistent with the formation of the diazene, as they appear as two sets of aromatic doublets at 7.78 ppm and 7.60 ppm in which the more shielded one is related to the protons at the *tert*-butyl side while the more deshielded ones are assigned to the protons at the diazene side of the aromatic ring. Finally, the *p*-*tert*-butyl singlet is also identified at 1.38 ppm.

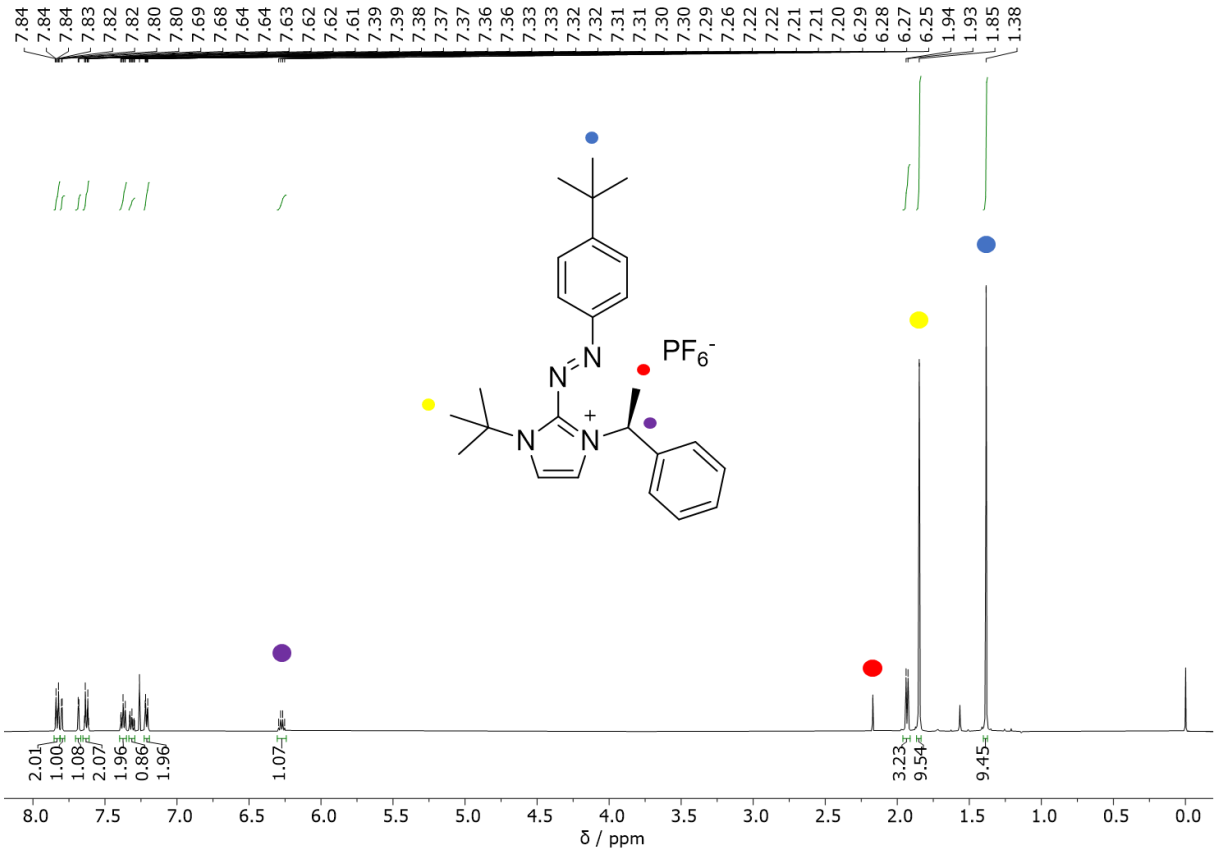

Figure 2.5. ^{1}H NMR spectrum of *E*-**1**; $CDCl_3$, 500 MHz, 298K.

An analogous assignment was carried out for the resonances observed in the ^{1}H NMR spectrum of *E*-**2** (**Figure 2.6**). A similar pattern to that of *E*-**1** could be observed, with minor variations in the chemical shift values due to the stronger electron donating methoxy group and with the replacement of the *p*-*tert*-butyl singlet with the singlet at 3.96 ppm, assigned to the *p*-methoxy substituent. Additionally, for both *E*-**1** and *E*-**2**, the presence of the hexafluorophosphate counterion was confirmed by the presence of the corresponding large doublet in their ^{19}F NMR spectra (**Figure 2.7**).

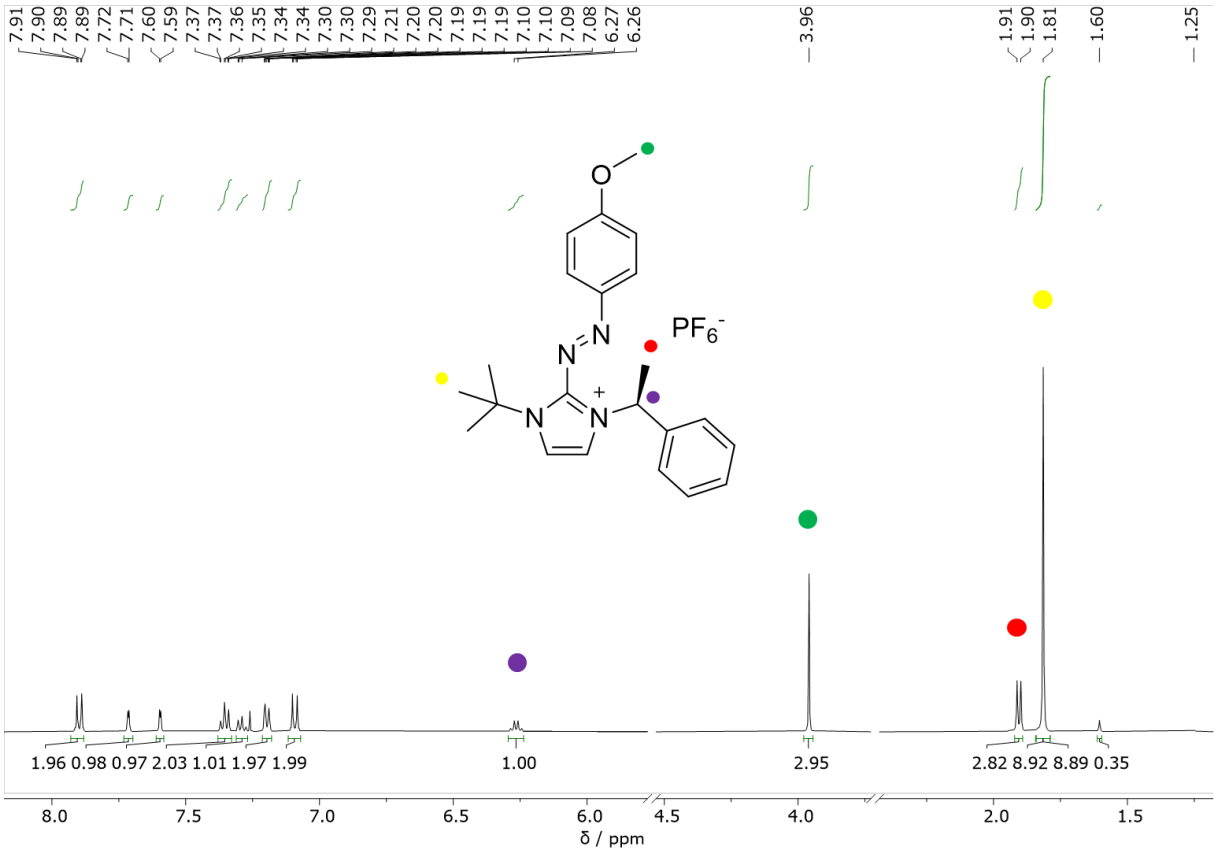

Figure 2.6. ^{1}H NMR spectrum of *E*-**2**; $CDCl_3$, 500 MHz, 298K.

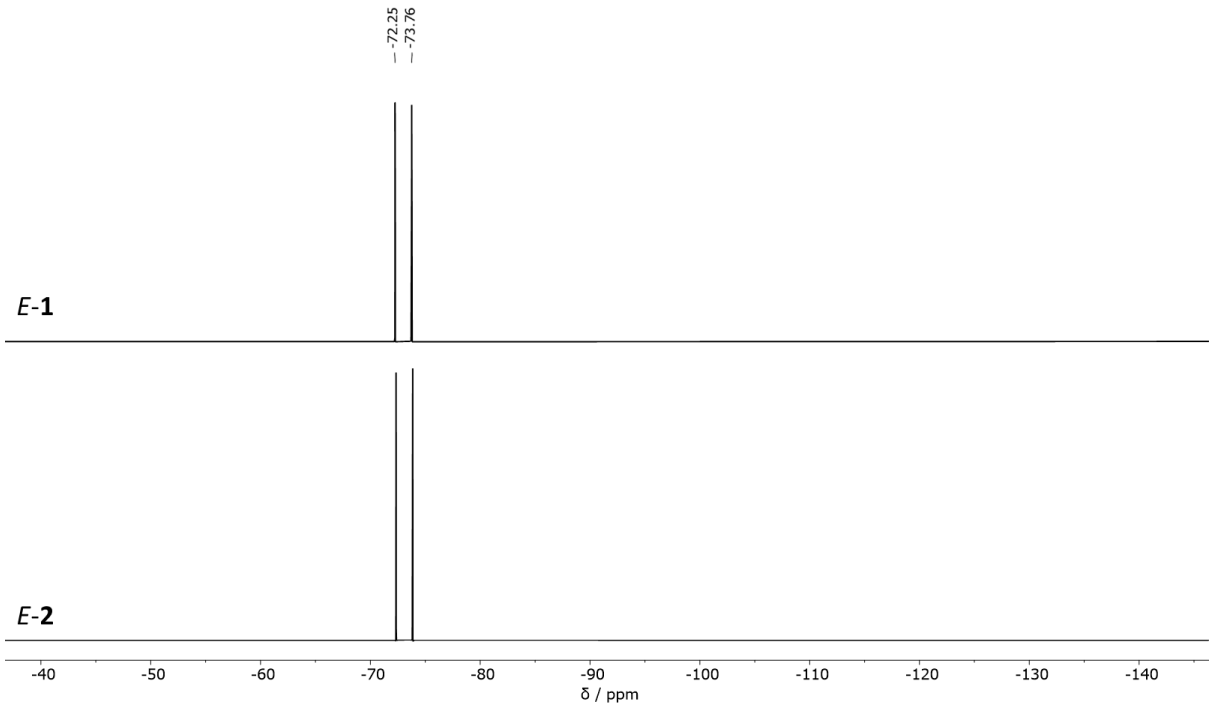

Figure 2.7. ^{19}F NMR spectra of *E*-**1** and *E*-**2**; $CDCl_3$, 500 MHz, 298K.

In order to work as molecular rotary motors, compounds *E*-**1** and *E*-**2** must necessarily be able to isomerize upon irradiation with light at a suitable wavelength. This requirement prompted their photophysical characterization by means of UV-Vis spectroscopy.

The absorption spectrum of compound **1** in $CHCl_3$ is reported in **Figure 2.8** and shows the typical spectral features of aryldiazene compounds: an intense π-π* band in the visible region (ε = 23000 M^{-1} cm^{-1} at 385 nm) which overlaps with the n-π* band that appears as a shoulder of the former. The strong UV band arises from the symmetry-allowed π-π* transition, while that in the visible region corresponds to the symmetry-forbidden *n*-π* transition.

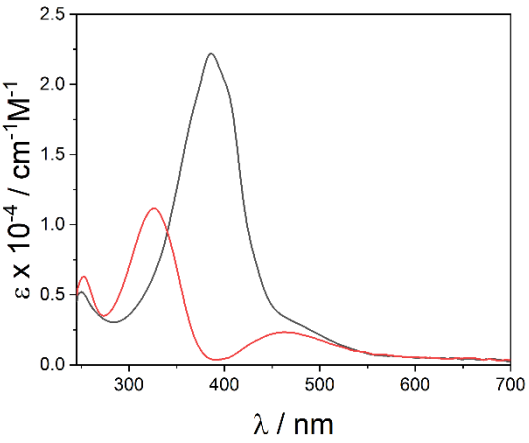

Figure 2.8. Absorption spectra of the *E* (black trace) and *Z* (red trace) isomers of compounds **1** in $CHCl_3$.

Irradiation at 365 nm of **1** produces appreciable spectral variations which are consistent with the $E \rightarrow Z$ isomerization and display a decrease of the main band in the UV range and the uprising of the band in the visible range. Moreover, the presence of isosbestic points at 341 nm and 508 nm suggests a clean transformation between the two species. Thus, excitation into the π-π* band with light results in a clean photoinduced isomerization, from the most stable *E*-form to the metastable *Z* -form, reaching a photostationary state (PSS) mainly composed by the photochrome *Z*-**1** (**Figure 2.9 a**). Additional photokinetic experiments were carried out on compound **1** under different irradiation wavelengths (**Figure 2.9 b,c**) to obtain the absorption spectrum of the pure *Z* isomer and quantify the photoisomerization quantum yields for the $E \rightarrow Z$ ($\Phi_{E \rightarrow Z}$) reaction. Since **1** is a new photochrome, the correct extrapolation of the theoretical absorption spectrum of the *Z*-form is of fundamental importance for a precise photochemical study of its properties. Interestingly, the major conversion of *E*-**1** into its metastable *Z*-form is obtained irradiating the sample at 405 nm (**Figure 2.9 b**).

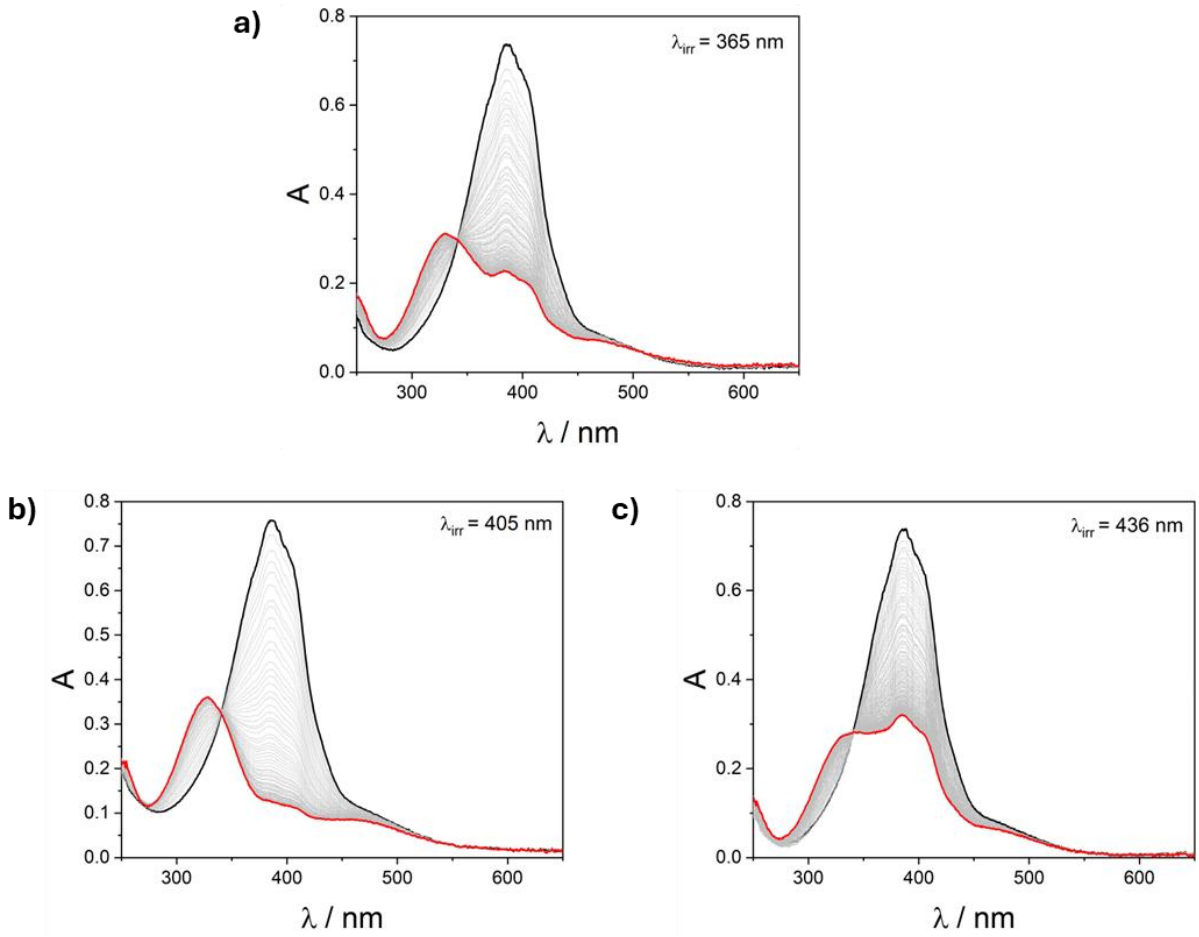

Figure 2.9. Absorption variations of a 3.4×10^{-5} M solution of *E*-**1** in $CHCl_3$ (black trace) upon irradiation at (a) 365 nm, (b) 405 nm and (c) 436 nm until PSS is reached (red trace).

After exhaustive irradiation with UV light (365 nm), spontaneous $Z \rightarrow E$ thermal isomerization was monitored at room temperature and reached completion after 60 min with a rate constant of 3.79×10^{-3} s^{-1} (**Figure 2.10 b**). The photochemical back-isomerization was tested upon irradiation at 436 nm of a solution of *E*-**1**, which resulted in a PSS mainly composed by the chromophore in its *E* configuration (**Figure 2.10 a**).

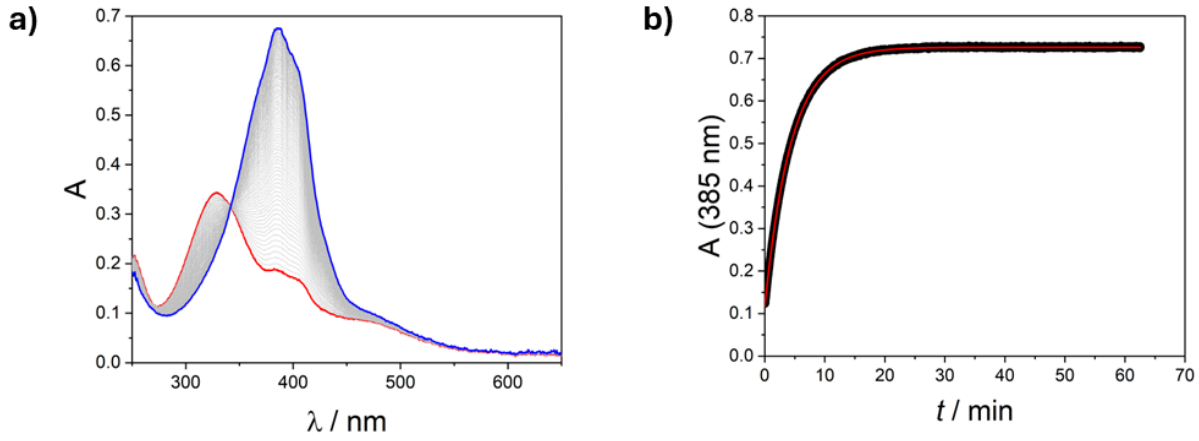

Figure 2.10. a) Thermal isomerization of a 3.4 × 10^{-5} M solution of *Z*-**1** in $CHCl_3$ at 298 K after exhaustive irradiation at 365 nm (red trace) until total recovery of the *E* isomer (blue trace); b) Absorption changes at 385 nm (black dots) together with data fitting (red trace).

The results of the photochemical characterization of compound **1** are summarized in **Table 1.**

Table 1. UV-vis photophysical and photochemical data of compound **1** ($CHCl_3$, 298 K).

Compound	Absorption		Isomerization			
	λ_{max} / nm	ε / M^{-1} cm^{-1}	λ_{irr} / nm	$\Phi_{E\rightarrow Z}$	*Z*:*E* PSS/%	k_Z^{Δ} /s^{-1}
E-**1**	385	23000	365	0.23	30:70	3.79 × 10^{-3}
			405	0.30	15:85	
			436	0.18	45:55	

The absorption spectrum of compound **2** is reported in **Figure 2.11**. Differently from what observed for **1**, the spectrum shows an intense band in the UV region (ε = 29000 M^{-1} cm^{-1} at 408 nm) and a weaker and broader tail in the visible region (ε = 12000 M^{-1} cm^{-1} at 461 nm). The notable red shift of the π-π* band is likely due to the presence of the methoxy EDG in the chromophore that provides a 25 nm shifted λ_{max} with respect to **1**.

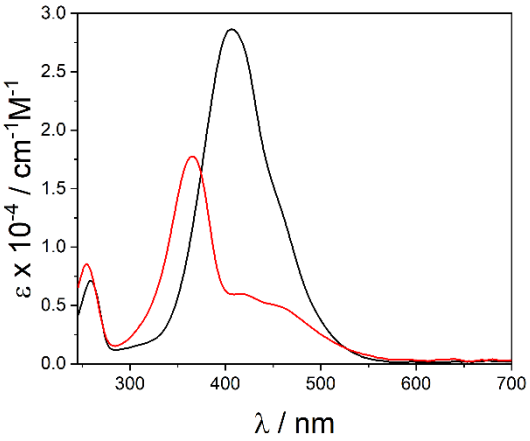

Figure 2.11. Absorption spectra of the *E* (black trace) and *Z* (red trace) isomers of compound **2**; $CHCl_3$, 298 K.

Irradiation with UV light (365 nm) of compound **2** promotes *E* → *Z* isomerization, leading to a PSS in which the main component is *E*-**2** (**Figure 2.11 a**). In contrast, exhaustive irradiation of *E*-**2** with visible light (405 nm and 436 nm) efficiently produces a PSS richer in *Z*-chromophore (**Figure 2.11 b,c**).

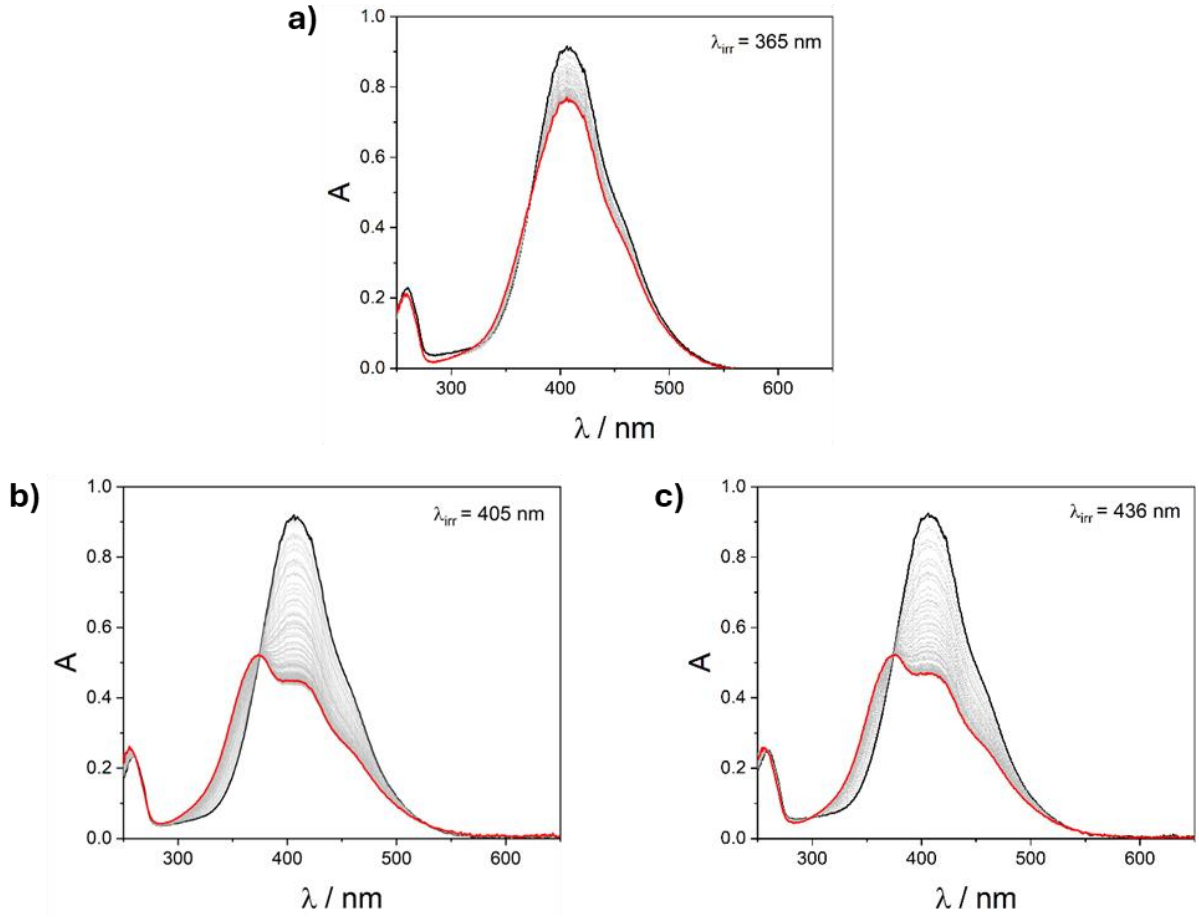

Figure 2.12. Absorption variations of a 3.5 × 10^{-5} M solution of *E*-**2** (black trace) in $CHCl_3$ at 298 K upon irradiation at (a) 365 nm, (b) 405 nm and (c) 436 nm until PSS is reached (red trace).

The thermal back-isomerization reaction was monitored in the dark and resulted completed in 10 min with a rate constant of 2.47 × 10^{-2} s^{-1} (**Figure 2.13 b**). Hence, the thermal stability of *Z*-**2** is lower than that observed for *Z*-**1**. An overview of the photochemical study of **2** is provided in **Table 2.**

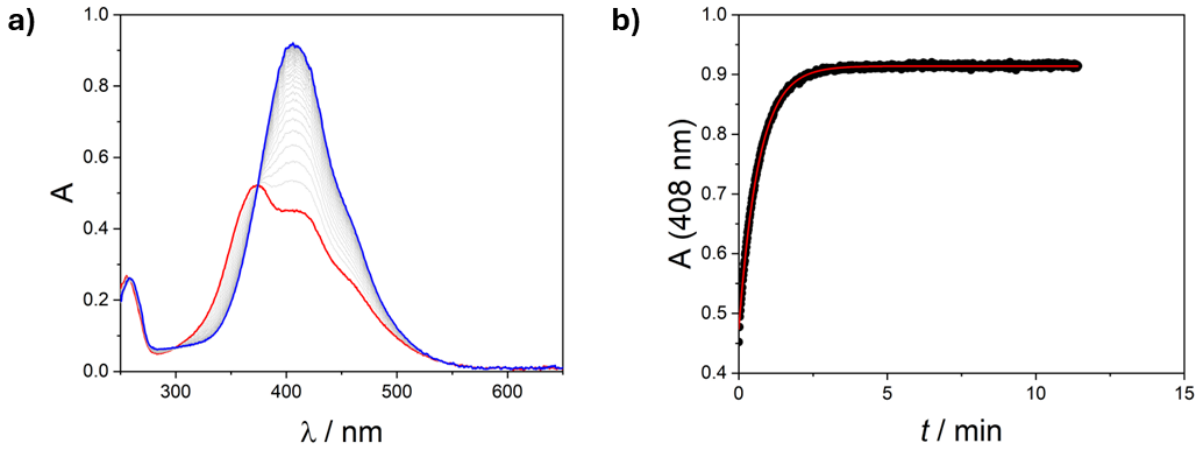

Figure 2.13. a) Thermal isomerization of a 3.5 × 10^{-5} M solution of *Z*-**2** in $CHCl_3$ at 298 K after exhaustive irradiation at 405 nm (red trace) until total recovery of the *E* isomer (blue trace); b) Absorption changes at 408 nm (black dots) together with data fitting (red trace).

Table 2: UV-vis photophysical and photochemical data of compound **2** ($CHCl_3$, 298 K).

Compound	Absorption		Isomerization			
	λ_{max} /nm	ε / M^{-1} cm^{-1}	λ_{irr} / nm	$\Phi_{E\rightarrow Z}$	*Z*:*E* PSS/%	k_Z^{Δ} /s^{-1}
***E*-2**	408	29000	365	0.33	80:20	2.47×10^{-2}
			405	0.52	36:64	
			436	0.17	40:60	

The results of the photochemical studies carried out on **2** may be rationalized as follows: since the imidazolium cations can be considered as an electron acceptor from an electronic point of view, **2** may be considered as *push-pull* system thanks to the presence of the methoxy EDG. As a matter of fact, its photochemical behavior is in line with the one commonly observed for *push-pull* azobenzene-derived systems. Literature studies report that the presence of a strong electron-donor and a strong electron-acceptor in the 4- and 4'- positions of the two phenyl rings of the azobenzene decreases the energy of π-π* state so that the n-π* and π-π* transitions are nearly degenerate in energy and take place in the visible region. It is also widely reported that *push-pull* azobenzene compounds show an extremely fast thermal isomerization.

To expand the potential of the prepared diazene compounds to the aqueous environment, the hexafluorophosphate anion of *E*-**1** was replaced by a Chloride counterion. To do so, *E*-**1** was dissolved in methanol and passed through a column filled with beads of ion exchange resin made of polystyrene chains bearing appended quaternary alkylammonium chloride groups. Upon repeated elution, *E*-**1** was quantitatively converted to its water-soluble chloride version *E*-**3**. NMR spectroscopic characterization of the latter confirmed the quantitative anion exchange through the disappearance of the hexafluorophosphate doublet in the ^{19}F spectrum, while the expected pattern of resonances was retained in the ^{1}H spectrum (**Figure 2.14**).

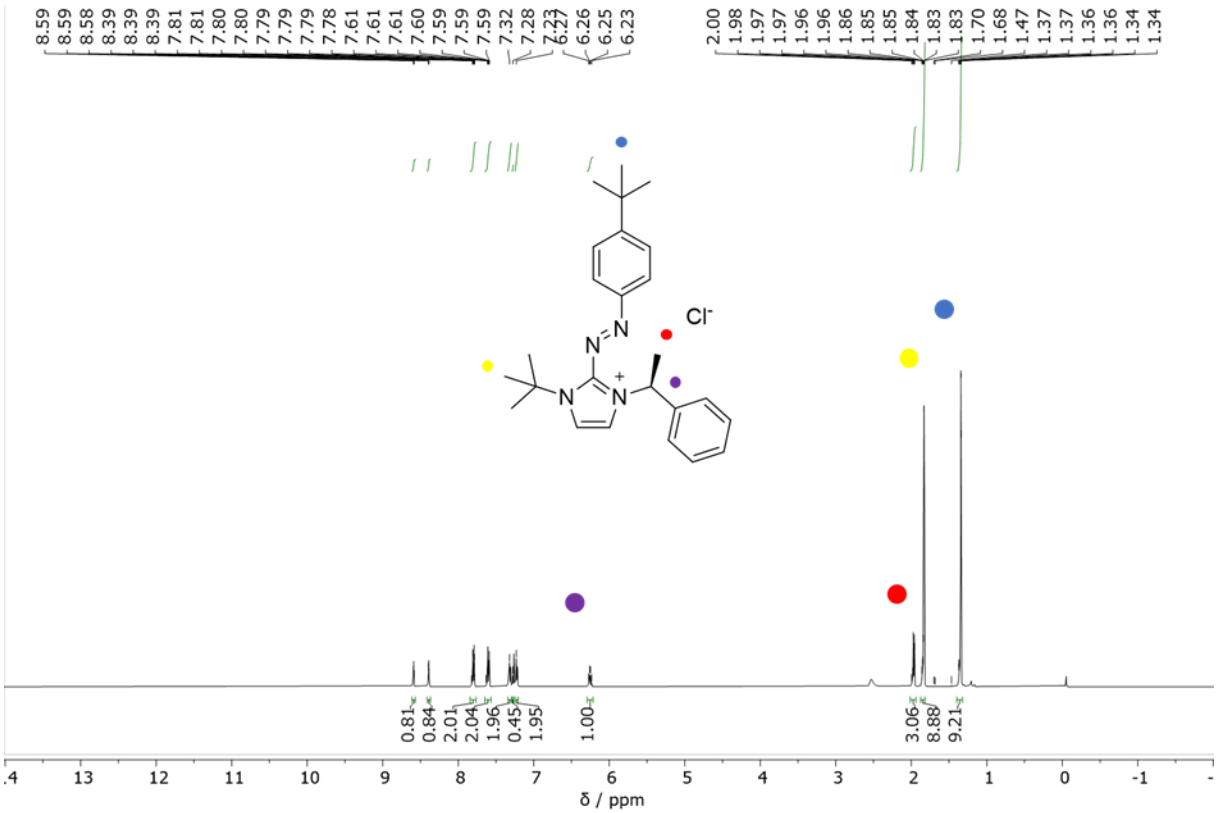

Figure 2.14. ^{1}H spectrum of *E*-**3**; 500 MHz, $CDCl_3$, 298 K.

Once confirmed the good solubility of *E*-**3** in water, its photochemical properties were assessed to validate its potential as a light-driven molecular motor to work in aqueous environment. The absorption spectrum of *E*-**3** in water is reported in **Figure 2.15.** and is comparable with that of *E*-**2**,: in the UV region it is possible to identify an intense π-π* band (ε = 20000 M^{-1} cm^{-1} at 376 nm) and a weaker and broader tail in the visible region (ε = 1700 M^{-1} cm^{-1} at 465 nm). The counterion exchange from hexafluorophosphate to chloride and, subsequently, of the solvent (from $CHCl_3$ to water) did not significantly affect the arylazoimidazolium chromophore.

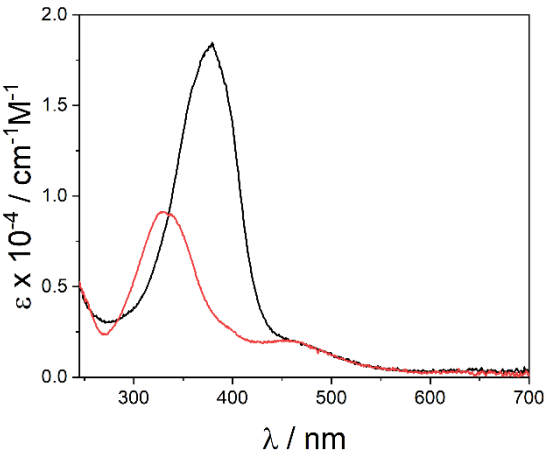

Figure 2.15. Absorption spectra of the *E* (black trace) and *Z* (red trace) isomers of compound **3** in water.

Upon irradiation at 365 nm (**Figure 2.16 a**), **3** undergoes an efficient $E \rightarrow Z$ isomerization with spectral features comparable with those of related compound **1**, but with lower photoisomerization quantum yield of $\Phi_{E \rightarrow Z} = 0.12$. Additionally, the PSS reached is composed by 60% of the photochrome in its *Z* configuration. As previously reported for **1**, the major conversion of *E*-**3** into its metastable *Z*-form is obtained by irradiating the sample at 405 nm (**Figure 2.16 b**).

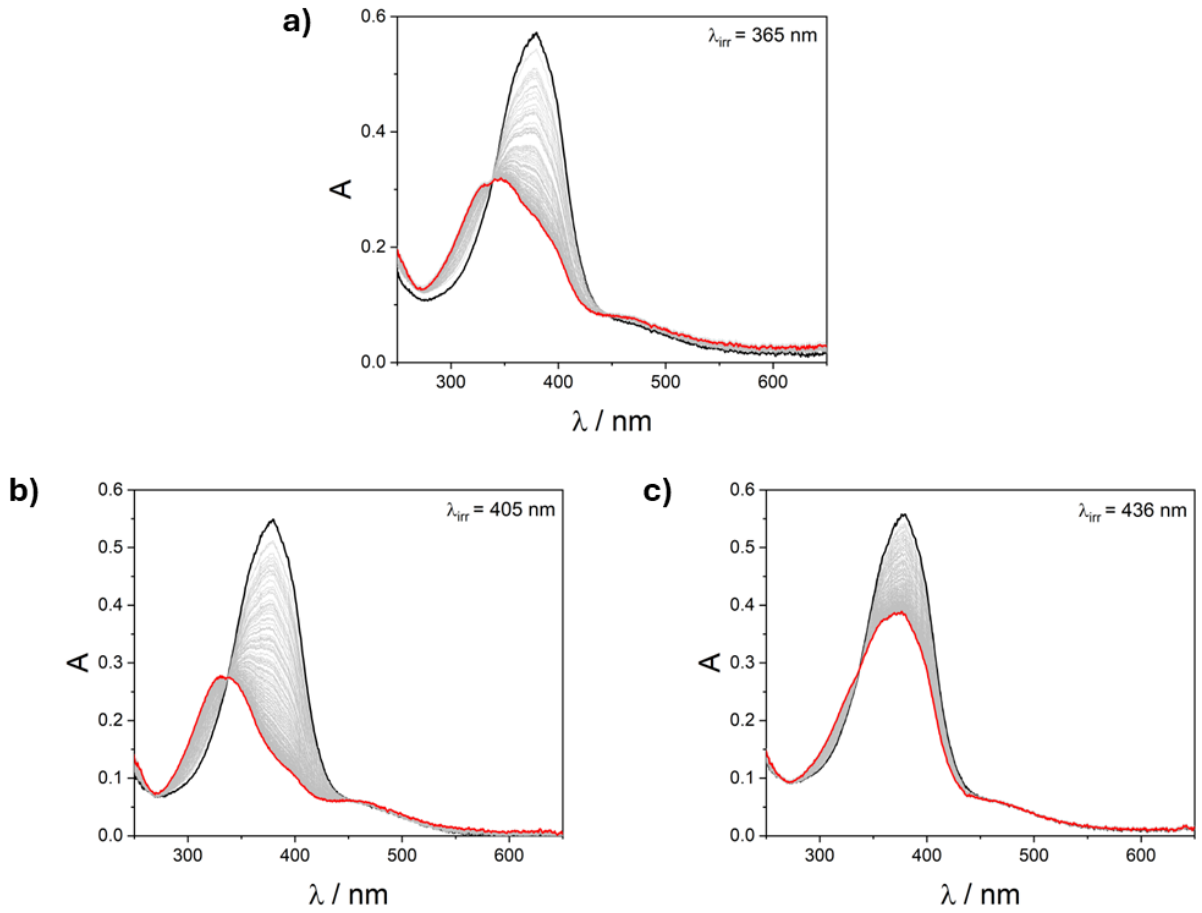

Figure 2.16. Absorption variations of a 3.05×10^{-5} M solution of *E*-**3** in H_2O (black trace) upon irradiation at (a) 365 nm, (b) 405 nm and (c) 436 nm until PSS is reached (red trace).

The back- isomerization was monitored by leaving *Z*-**3** in the dark at room temperature and after 100 min the process was completed with a rate constant of 1.13×10^{-3} s^{-1} (**Figure 2.17 b**). This increase in the thermal stability of the metastable *Z*-**3** compared to what previously observed in organic solvent for *Z*-**1** could be explained considering a possible stabilization of its polar *Z*-form thanks to the high polarity of the solvent in which the process is studied. The photochemical back-isomerization was tested upon irradiation at 436 nm of a solution of *E*-**3**, which resulted in a PSS mainly composed by the chromophore in its *E* configuration (**Figure 2.17 a**).

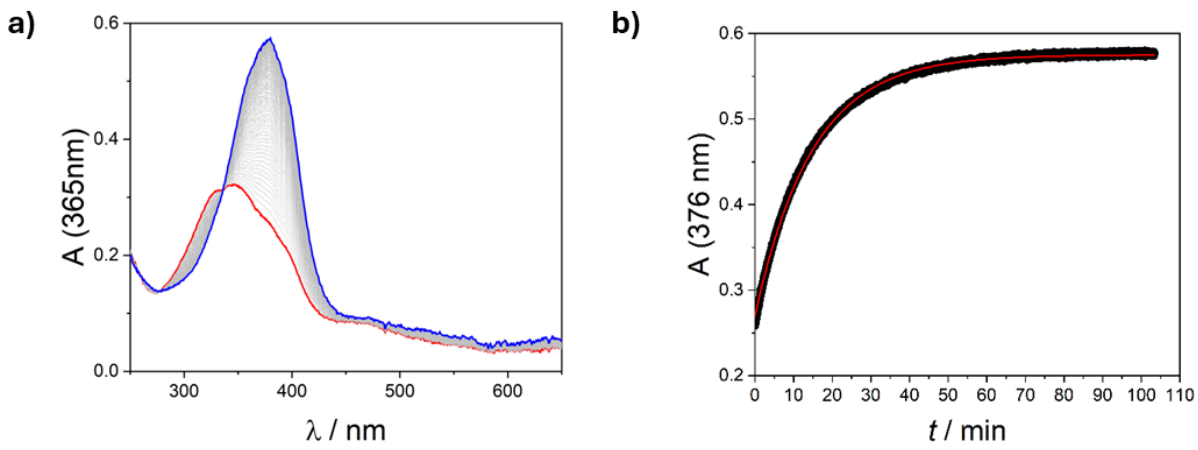

Figure 2.17. a) Thermal isomerization of a 3.05 × 10^{-5} M solution of *Z*-**3** in H_2O at 298 K after exhaustive irradiation at 365 nm (red trace) until total recovery of the *E* isomer (blue trace). b) Absorption changes at 376 nm (black dots) together with data fitting (red trace).

The complete photochemical characterization of compound **3** is summarized in **Table 3**.

Table 3: UV-vis photophysical and photochemical data of compound **3** (H_2O, 298 K).

Compound	Absorption		Isomerization			
	λ_{max} / nm	ε / M^{-1} cm^{-1}	λ_{irr} / nm	$\Phi_{E\rightarrow Z}$	*Z*:*E* PSS/%	k_Z^{Δ} / s^{-1}
E-**3**	376	20000	365	0.12	40:60	1.13 × 10^{-3}
			405	0.14	20:80	
			436	0.15	65:35	

Once the synthesis and characterization of the molecular motors was completed, compounds *E*-**1** and *E*-**2** were subjected to an *in situ* photochemical NMR study to validate their ability to undertake directionally biased rotary motion. The study involves the irradiation of the sample solution directly inside the NMR tube in the spectrometer probe by means of a quartz optical fiber thread, with real time monitoring through the acquisition of an array of ^{1}H NMR spectra. The first compound to be tested was *E*-**1**, as a 10 mM $CDCl_3$ solution irradiated at 365 nm. The experiment was run at 218 K to minimize the impact of the thermal back-isomerization, whose $t_{½}$ slows down from <10 min at 298 K to 59 h at 218 K. Irradiation of *E*-**1** provides a PSS mixture in which it is possible to identify three independent sets of resonances (**Figure 2.18**). The first corresponds to the starting *E*-isomer, while the remaining two are related to the diastereomeric pair of *Z*-isomers obtained upon photoisomerization. Interestingly, the resonances related to the chiral fragment of the *Z*-isomers appear considerably shielded, with the benzylic CH quartets at 4.13 ppm and 4.38 ppm and the methyl doublets at 1.03 ppm and 1.91 ppm.

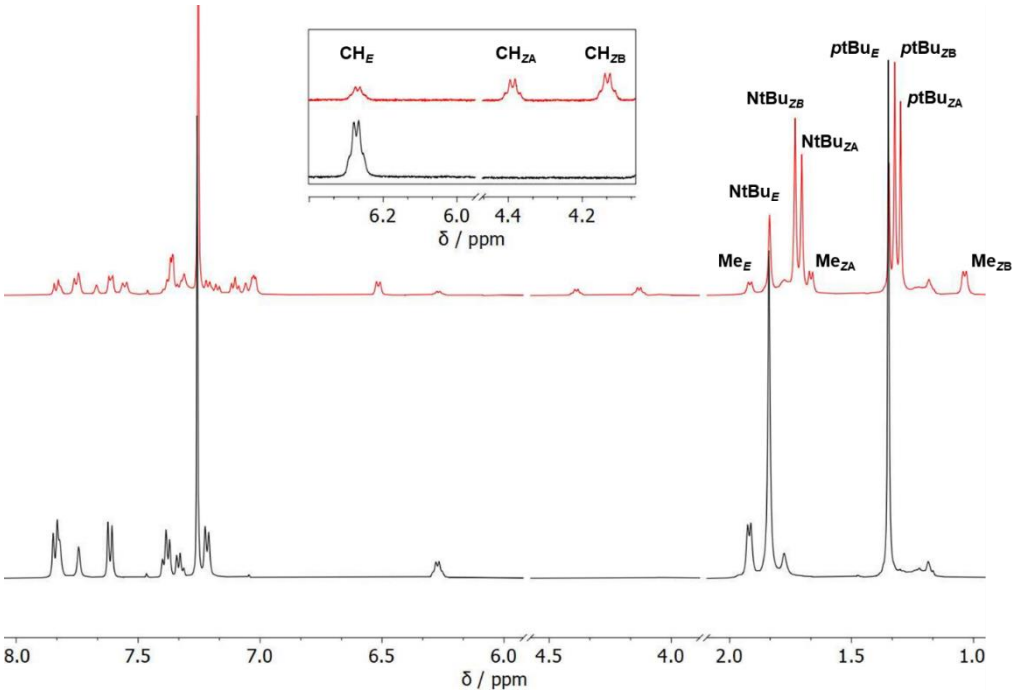

Figure 2.18. ^{1}H NMR spectra of *E*-**1** (black trace) and of the PSS mixture obtained upon irradiation at 365 nm (red trace); $CDCl_3$, 500 MHz, 218 K.

The dynamic interconversion between the *E*- and *Z*-isomers of **1** defines a triangular closed reaction network consisting of two photochemical isomerization reactions, [*E*-**1**] ⇄ [Z_A-**1**] and [*E*-**1**] ⇄ [Z_B-**1**], and the thermal [Z_A-**1**] ⇄ [Z_B-**1**] interconversion (**Figure 2.19 a**). The diastereomeric nature of the *Z*-isomers confers them different stability and potentially different photochemical reactivity.

Monitoring the evolution of the Z-species over time during the irradiation, thus the photokinetic process, two scenarios can be envisaged:
Thermal control – should the thermal [Z_A-**1**] ⇄ [Z_B-**1**] equilibration be faster than the photochemical processes, at each acquired point the system would be equilibrated and suspension of irradiation would lead to no changes in the relative ratio between the diasteromers;
Photochemical control – should the photochemical reactions be faster than the thermal equilibration, the dissipative non-equilibrium state sustained upon continuous illumination would be lost upon suspension of the illumination and the system would equilibrate thermally in the dark to the relative stability ratio between the *Z*-species.

In both the previous cases the thermal back-isomerization in the dark is considered negligible as it is by far the slowest process. The experimental photokinetic experiment is reported in figure X and shows how upon irradiation the system evolves to a PSS mixture composed of a 57:43 ratio between [Z_B-**1**] and [Z_A-**1**] (14% *d.e.*, **Figure 2.19 b**, yellow background). Upon interruption of the illumination, the diastereomers undergo thermal equilibration over time reaching a plateau ratio of 55:45 (10% *d.e.*, **Figure 2.19 b**, grey background), while resuming the 365 nm illumination restores the original 57:43 ratio. These results provide important information to understand the behavior of the system. Under constant irradiation the concentrations of [Z_B-**1**] and [Z_A-**1**] are continuously driven away from

their equilibrium value, therefore the system is under photochemical control. Additionally, the most stable diastereomer [Z_B-**1**] is accumulated beyond its equilibrium concentration during the dissipative operation, thus indicating that the processes leading to its formation (*i.e*. the photochemical [*E*-**1**] ⇄ [Z_B-**1**] isomerization) or to the disappearance of [Z_A-**1**] (*i.e*. the photochemical [*E*-**1**] ⇄ [Z_B-**1**] back-isomerization) generate kinetic asymmetry within the closed network. Overall, the result is a net directional travel along the network in a clockwise fashion encompassing the sequence i) [*E*-**1**] → [Z_B-**1**], ii) [Z_B-**1**] → [Z_A-**1**] and iii) [Z_A-**1**] → [*E*-**1**] (**Figure 2.19 c**). Importantly, since each of the three species composing the network is associated to a different spatial position of the arylazo group, the directional travel along the network corresponds to a net directional rotary motion across space.

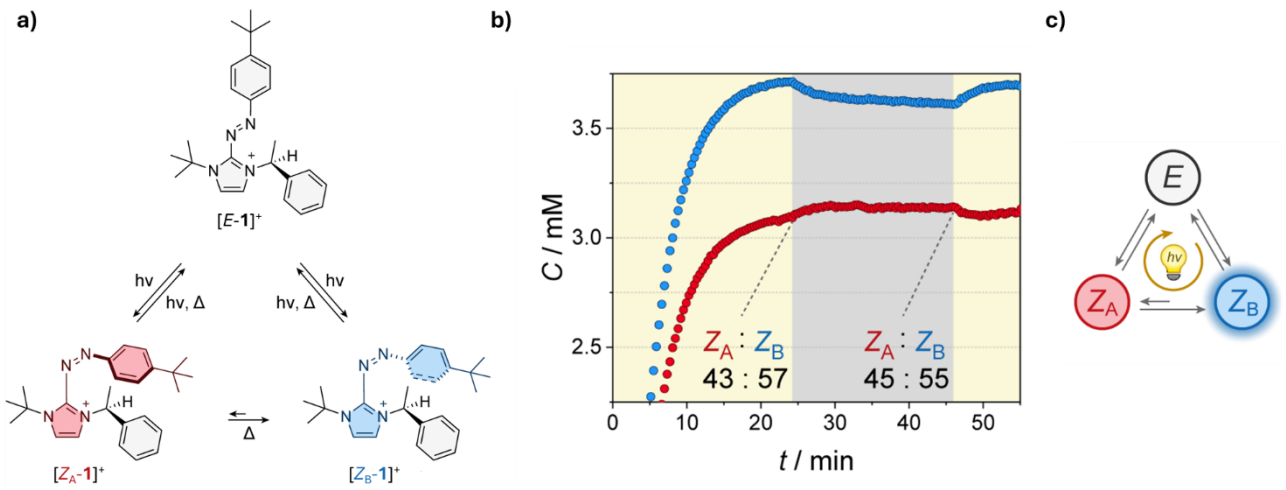

Figure 2.19. a) Triangular closed reaction network displaying the functioning of motor **1**; b) *In situ* NMR photokinetic experiment, c) Overall directionally biased travel; $CDCl_3$, 500 MHz, 218 K.

The successful results obtained for *E*-**1** prompted the related study of *E*-**2**, with the advantage of using fully visible light due to the red-shift of the absorption maximum of this push-pull photochrome. As such, a 10 mM solution of *E*-**2** in $CDCl_3$ was irradiated at 405 nm at 218 K. This time, the PSS composition was even more shifted toward one of the two *Z*-diastereomers, with a relative ratio of 60:40 (**Figure 2.20 a**). However, the photokinetic experiment for *E*-**2** displayed no variation in the diastereomer ratio upon suspension of illumination (**Figure 2.20 b**, grey background). This can be rationalized considering that the system is under thermal control due to the less sterically hindered methoxy substituent, leading to a much faster thermal equilibration, combined with the faster thermal back-isomerization likely opposing the forward photochemical isomerization.

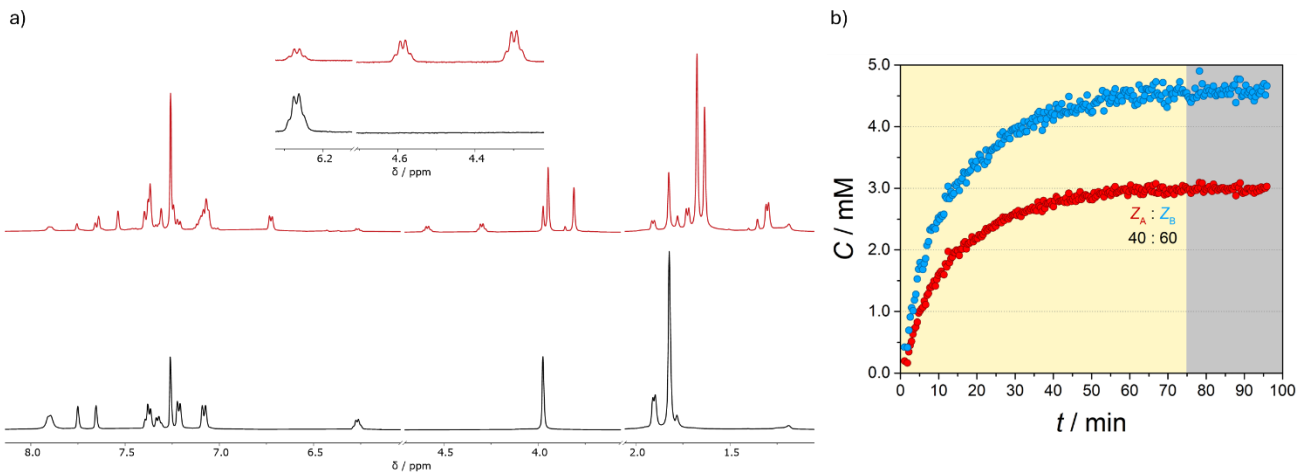

Figure 2.20. a) ^{1}H NMR spectra of *E*-**2** (black trace) and of the PSS mixture obtained upon irradiation at 405 nm (red trace); b) *In situ* NMR photokinetic experiment; $CDCl_3$, 500 MHz, 218 K.

3. CONCLUSIONS AND OUTLOOK

Artificial molecular motors are at the forefront of research in nanotechnology, as their ability to perform work makes them suitable for application in smart materials and responsive systems, and in this perspective light-operated molecules have clear advantages over their chemically and electrically driven counterparts. However, the reported classes of photochemical molecular rotary motors present important intrinsic limitations hindering their implementation.

To push forward the boundaries of research in this scientific area, this thesis introduces azoimidazolium cations as an innovative class of light-driven molecular rotary motors. Thus, azoheteroarene compounds *E*-**1** and *E*-**2**, differing in the *tert*-butyl or methoxy *p*-arylazo substituent, were efficiently isolated through a minimalistic, straightforward and easily scalable synthetic procedure and their identity was confirmed by NMR spectroscopic analysis.

From a photochemical point of view, motors *E*-**1** and *E*-**2** present the characteristic features of diazene derivatives, with a pronounced 25 nm red shift in the absorption maximum of *E*-**2** due to its push-pull nature. Light irradiation at an appropriate wavelength, 365 nm for *E*-**1** and 405 nm for *E*-**2**, successfully led to $E \rightarrow Z$ isomerization, supporting their molecular switching properties. The combination of photochemical isomerization and nonsymmetric substitution pattern at the imidazole ring endows these compounds with axial chirality which, coupled to the presence of a fixed chiral center, leads to the formation of two diastereomeric *Z*-isomers. The interconversion between the three motor isomers (*E*, Z_A and Z_B) defines a triangular closed reaction network which can in principle be travelled directionally due to either (or both) the different stability and photoreactivity of the *Z*-species. The closed network was investigated for both *E*-**1** and *E*-**2** through NMR spectroscopic studies conducted with *in situ* irradiation, providing different results at the defined operation conditions. In the case of *E*-**1**, the photochemical processes are faster than the thermal equilibration between the *Z*-species, the system is in photochemical control, and a preferred direction of travel along the closed network can be identified by monitoring the motor speciation under illumination and in the dark. In contrast, despite a more pronounced difference in the diastereomer stability, the minor steric hindrance of the methoxy group with respect to the *tert*-butyl one provides *E*-**2** with a faster thermal equilibration process. The system is therefore under thermal control and no variation in the motor speciation could be observed upon suspension of the irradiation.

To evaluate the potential of these molecules toward operation in water and aqueous systems, the hydrophilic motor *E*-**3** was also developed by simply replacing the hexafluorophosphate counterion with a chloride. Notably, the photoisomerization ability of *E*-**3** in water was not only retained but improved with respect to the lipophilic relative *E*-**1**, with a slower thermal back-isomerization process.

Overall, the present thesis poses solid bases on which this new class of photochromes will be developed, as it validates their potential as light-driven molecular rotary motors. Future studies will address some key features to improve their applicative potential, such as stability under constant illumination, improved diastereoselectivity between the *Z*-isomers, and enhanced red shift of the absorption maximum through expansion of the conjugated π system.

4. SUPPLEMENTARY DATA

4.1 Synthetic procedures

1- N-tert-butylimidazole

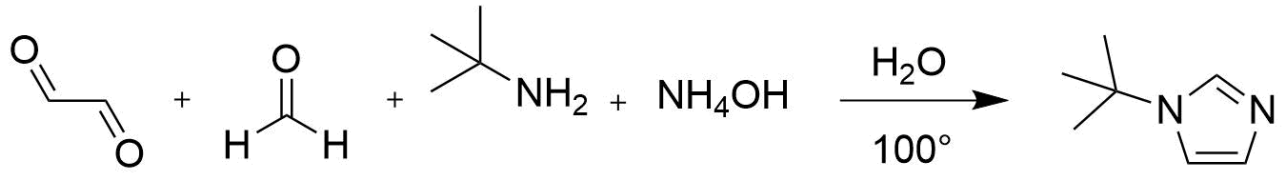

A three-necked flask is taken and placed under reflux (with air condenser) in an oil bath (T = 100 °C). Water (50 ml) was poured in and brought to the boil. Glyoxal (40wt%, 300 mmol, 1 eq) and formaldehyde (37wt%, 300 mmol, 1 eq) were placed in one dropping funnel, while *tert*-butylamine (300 mmol, 1 eq) and NH_4OH (29wt%, 300 mmol, 1 eq) were placed in another drip funnel. When the water was boiling, the two reagents were added dropwise anf left stirring for 30 min. The crude product was extracted with DCM and the organic fraction dried over anhydrous Na_2SO_4. After filtration, the solution was dried with a rotary evaporator. The *tert*-butylimidazole was purified by flash chromatography (silica gel, diethyl ether) and was isolated as a yellow oil. ^{1}H NMR (500 MHz, 298 K, Chloroform-*d*) δ 7.56 (t, J = 1.2 Hz, 1H, **3**), 7.01 (t, J = 1.2 Hz, 1H, **5**), 6.99 (t, J = 1.4 Hz, 1H, **4**), 1.51(s, 9H, **1**). ^{13}C NMR (101 MHz, 298 K; Chloroform-*d*) δ 134.4, 129.1, 116.3, 54.7, 30.6.

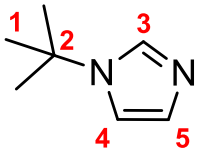

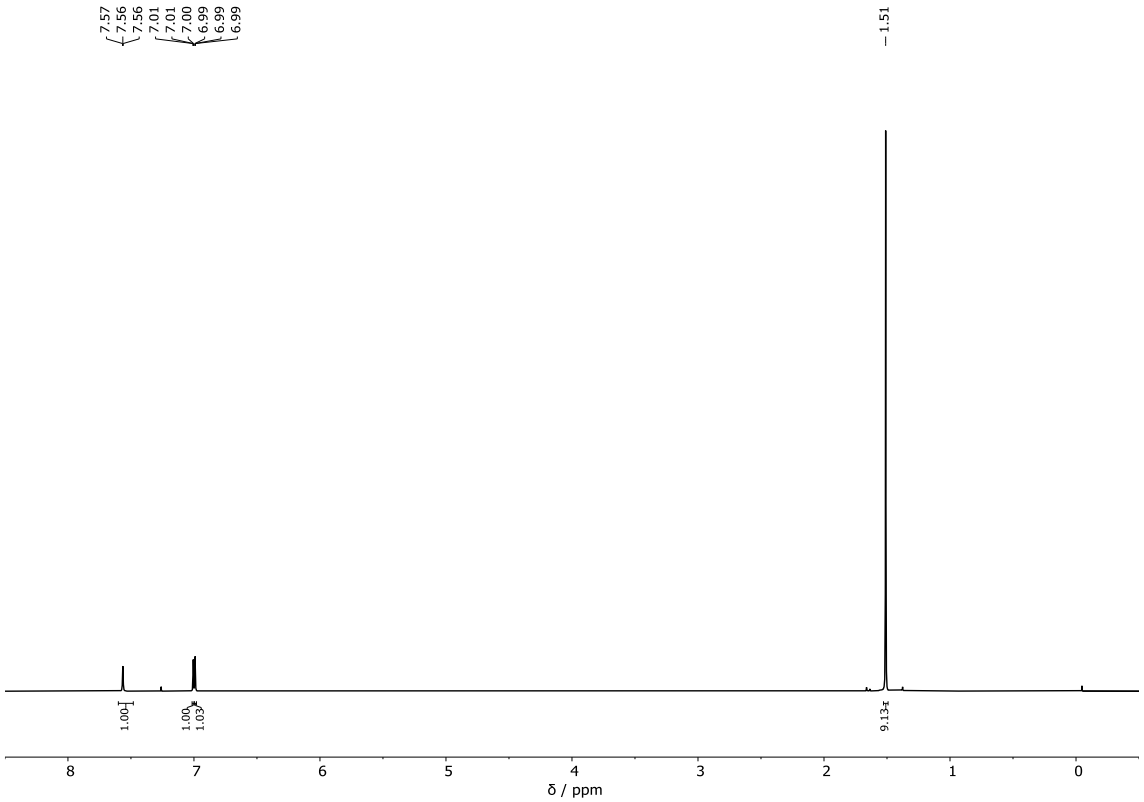

Figure 4.1. ^{1}H NMR spectrum of **3** (Chloroform-*d*, 298 K, 500 MHz).

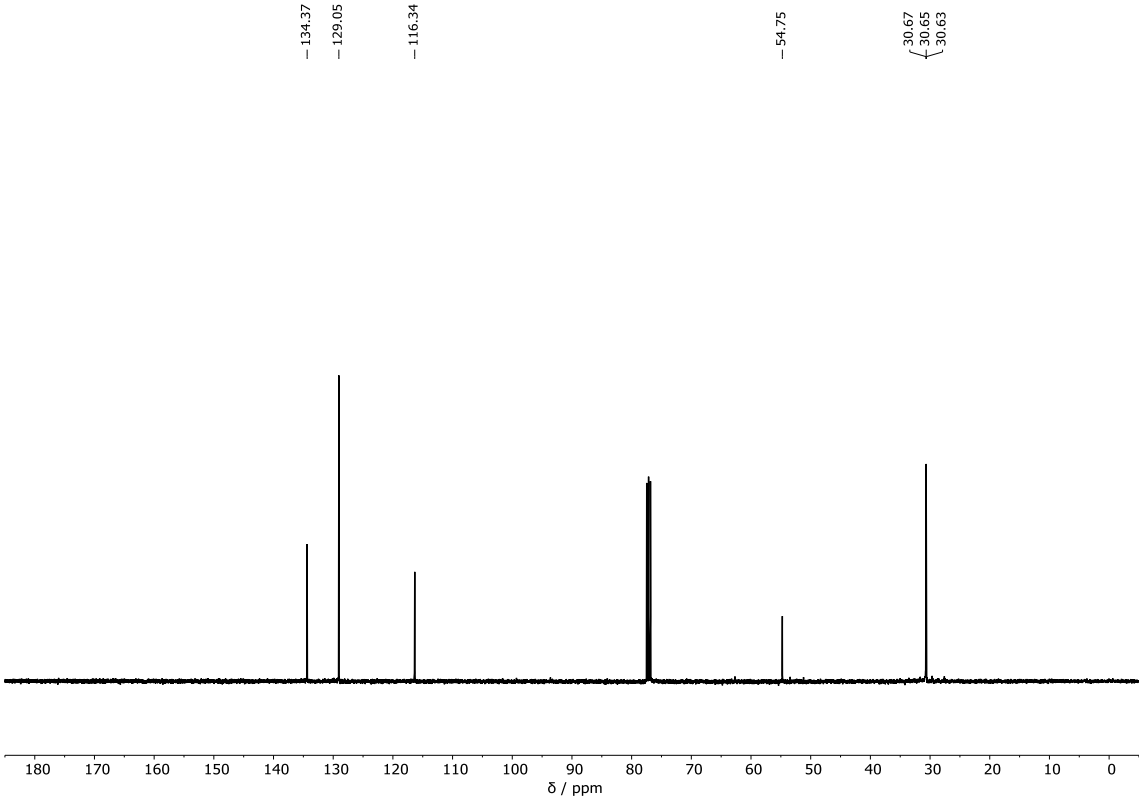

Figure 4.2. ^{13}C NMR spectrum of **3** (Chloroform-*d*, 298 K, 126 MHz)

2- (S)-(1-bromoethyl)benzene

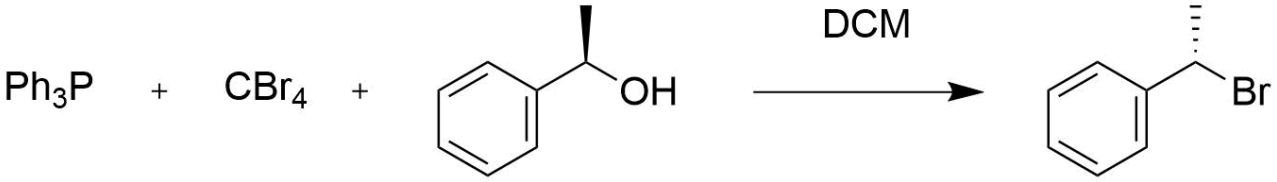

Triphenylphosphine (7.73 g) and CBr_4 (3.90 g) were dissolved in DCM (30 ml) and reacted for 40 min, until a red suspension formed. Then, (R)-1-phenylethanol (1,2g) was added dropwise, the reaction mixture cleared up and the reaction progress was monitored by TLC. The solution was dried with a rotary evaporator and the crude product was purified by flash chromatography (silica gel, diethyl ether) and obtained as a pale yellow oil. ^{1}H NMR (500 MHz, 298 K, Chloroform-*d*) δ 7.47 - 7.42 (m, 2H, **4**), 7.37 - 7.32 (m, 2H, **5**), 7.31 - 7.27 (m, 1H, **6**), 5.22 (q, *J* = 6.9 Hz, 1H, **1**), 2.06 (d, *J* = 6.9 Hz, 3H, **2**). ^{13}C NMR (126 MHz, 298 K, Chloroform-*d*) δ 143.4, 128.8, 128.5, 126.9, 49.7, 27.0.

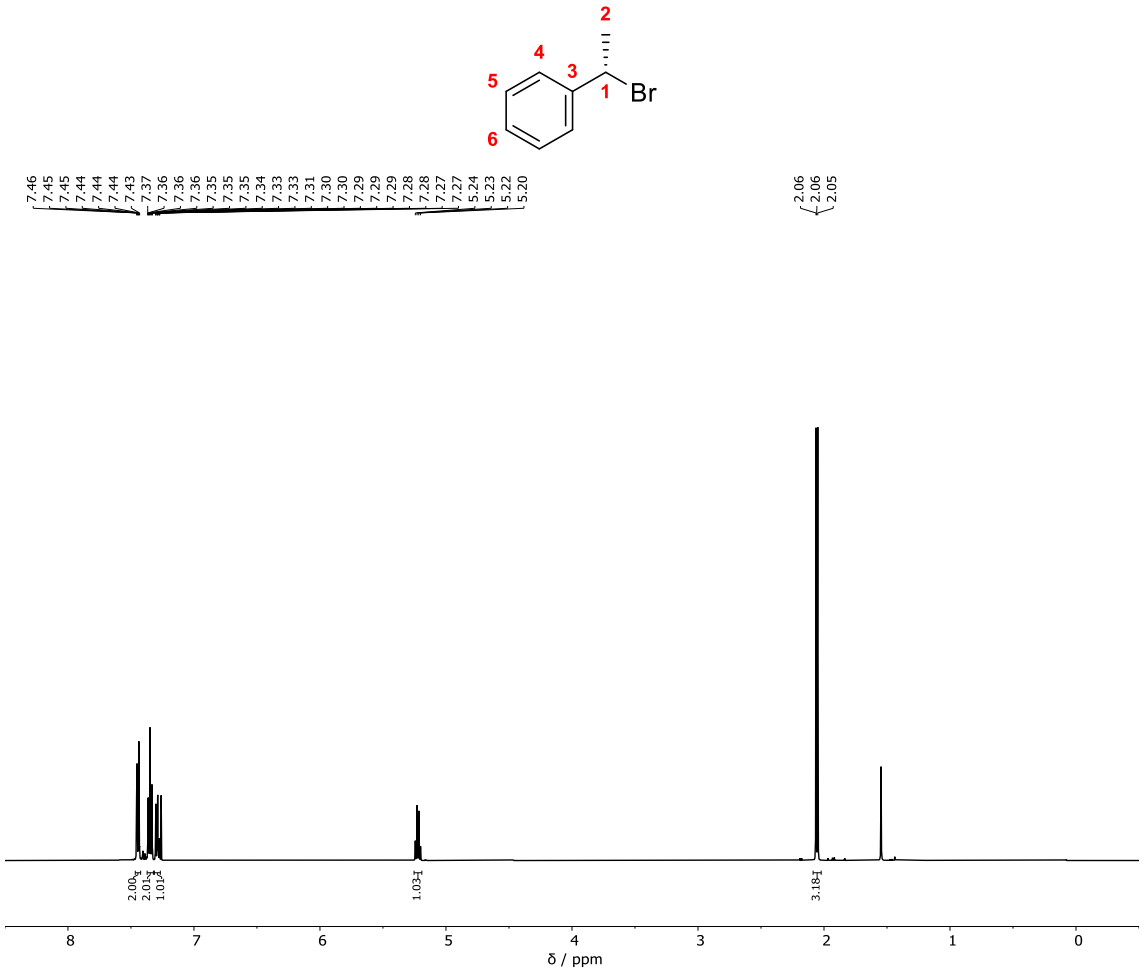

Figure 4.3. ^{1}H NMR spectrum of **5** (Chloroform-*d*, 298 K, 500 MHz).

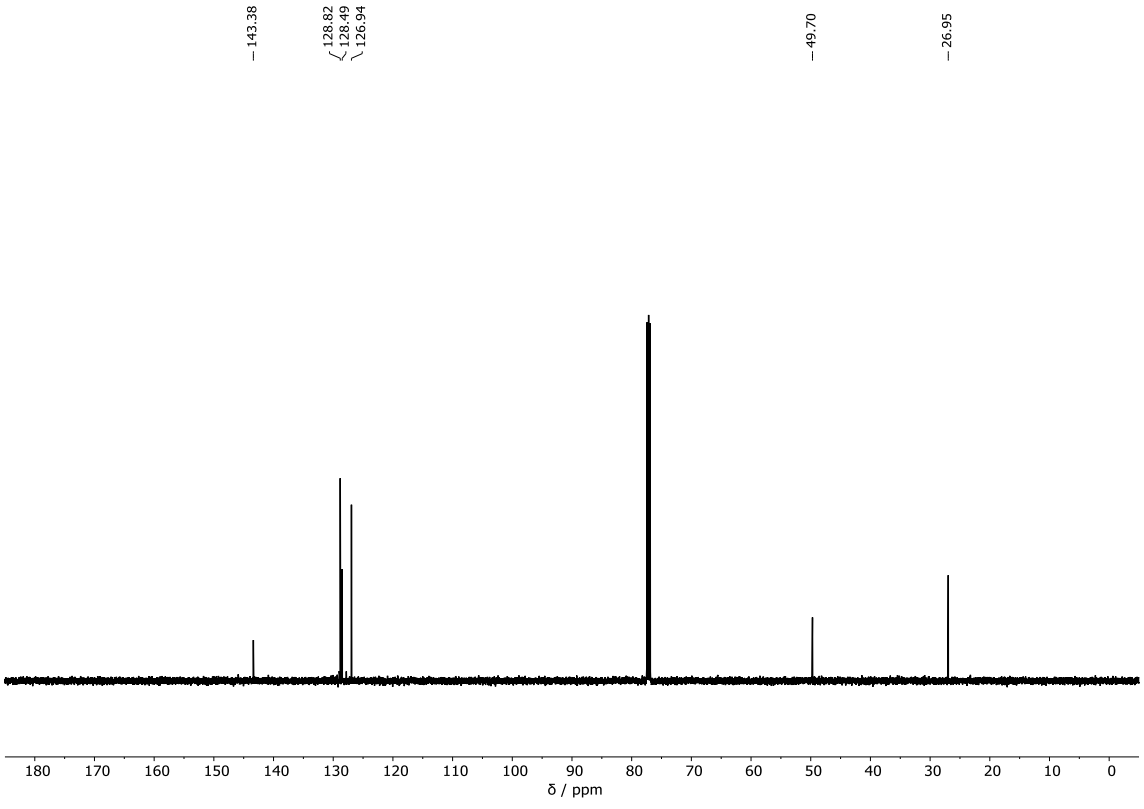

Figure 4.4. ^{13}C NMR spectrum of **5** (Chloroform-*d*, 298 K, 126 MHz).

3- (S)-1-(tert-butyl)-3-(1-phenylethyl)-1H-imidazol-3-ium bromide (A)

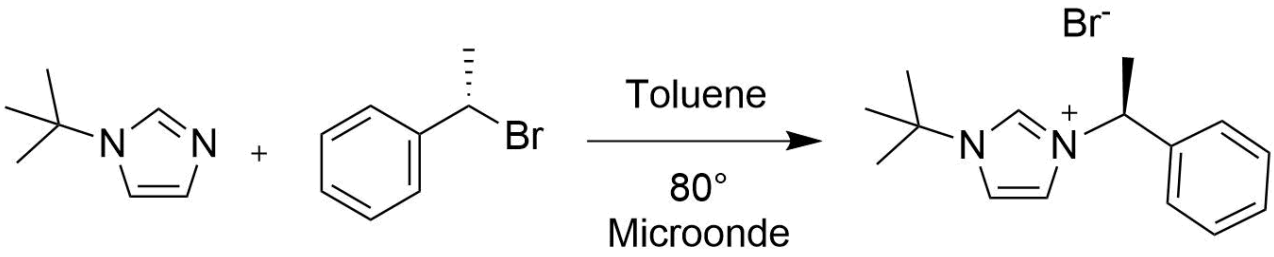

A

(S)-(1-bromoethyl)benzene (5,4 mmol, 1 eq) and an excess of N-tert-butylimidazole (0,805g, 6,48 mmol, 1,2 eq) were placed in a microwave vial. Then, toluene (50 ml) was added.

The closed vial was placed in the microwave at T=100°C for two hour. The product obtained in the vial is a clear brownish liquid and a brown solid. The solid was crushed and subsequently was washed with toluene and decanted several times. The solid was washed with ether and separated by filtering under vacuum. The solvent was removed under reduced pressure to provide the product. The product was obtained as light yellow powder. ^{1}H NMR (500 MHz, 298 K, Chloroform-*d*) δ 10.82 (d, *J* = 1.5 Hz, 1H, **3**), 7.58 - 7.52 (m, 2H, **9**), 7.40 (t, *J* = 1.9 Hz, 1H, **4**), 7.40 - 7.32 (m, 3H, **10**+**11**), 7.27 (d, *J* = 1.9 Hz, 1H, **5**), 6.38 (q, *J* = 7.1 Hz, 1H, **6**), 2.00 (d, *J* = 7.1 Hz, 3H, **7**), 1.73 (s, 9H, **1**). ^{13}C NMR (126 MHz, 298 K, Chloroform-*d*) δ 138.0, 135.7, 129.4, 129.4, 127.4, 119.9, 119.5, 60.8, 59.4, 30.3, 21.2.

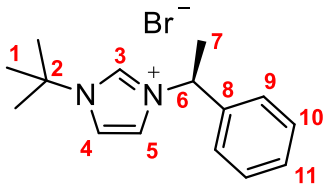

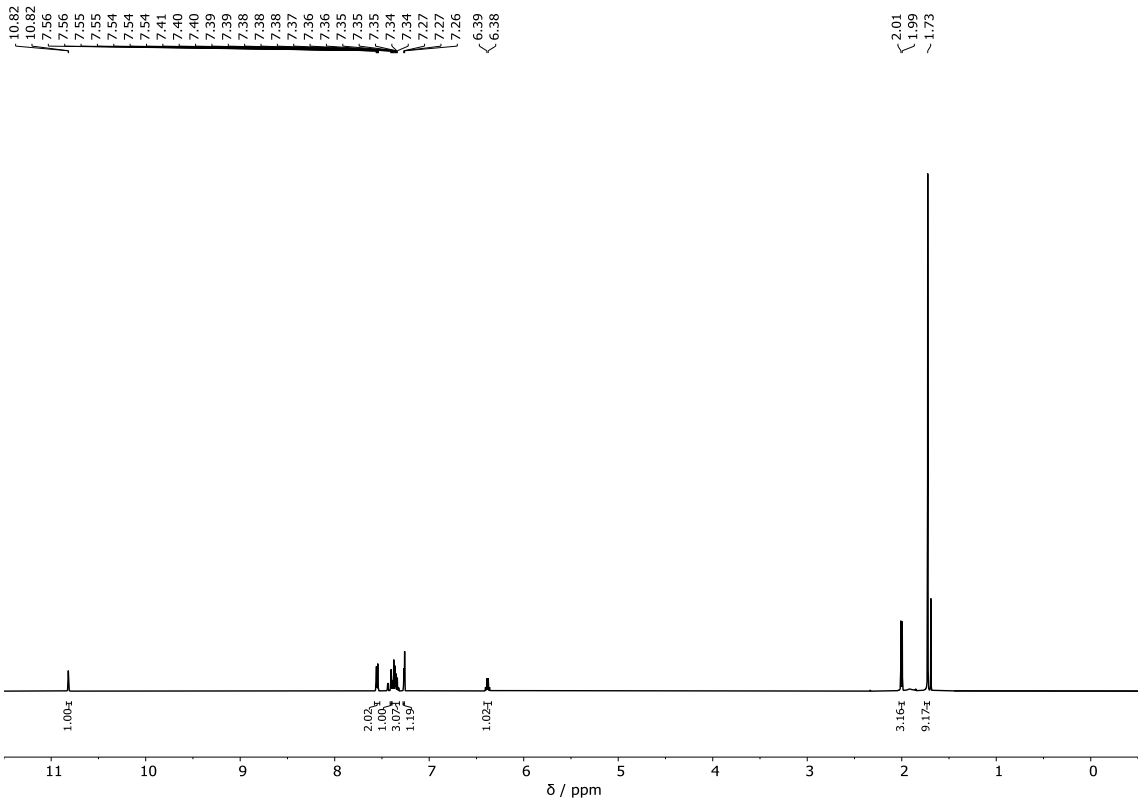

Figure 4.5. ^{1}H NMR spectrum of **A** (Chloroform-*d*, 298 K, 500 MHz).

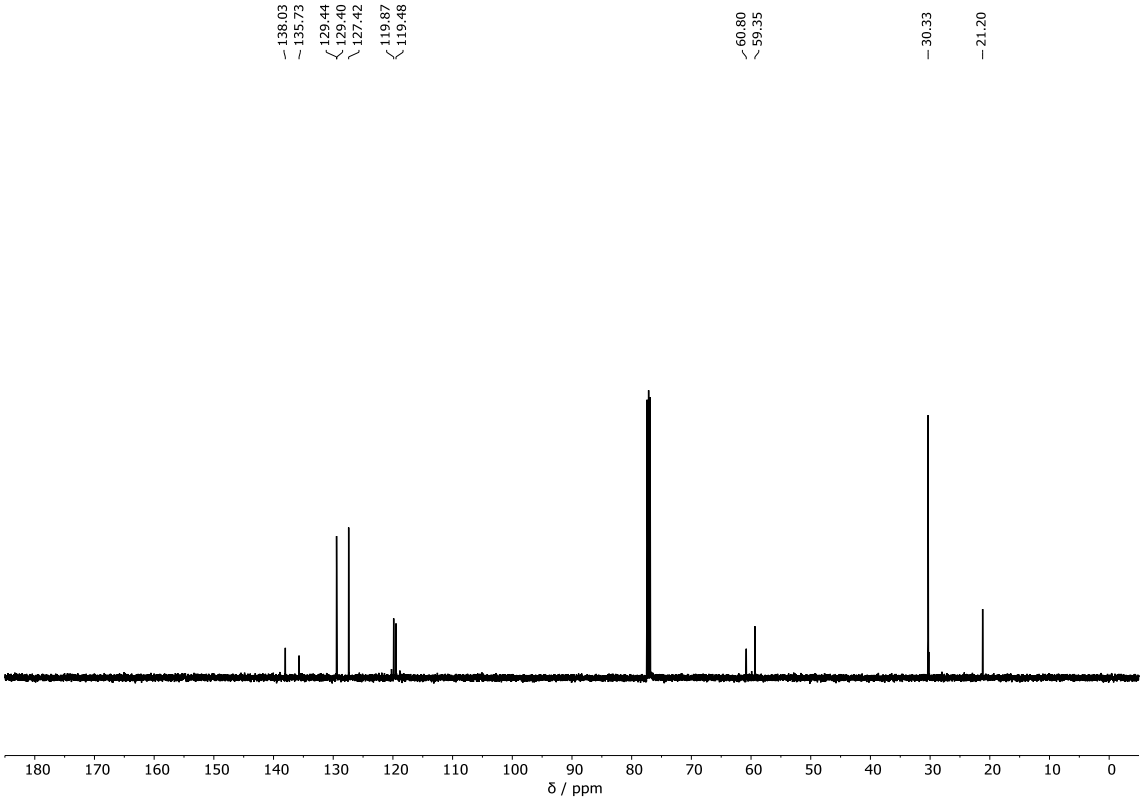

Figure 4.6. ^{13}C NMR spectrum of **A** (Chloroform-*d*, 298 K, 126 MHz)

4- (NHC)AgBr, B

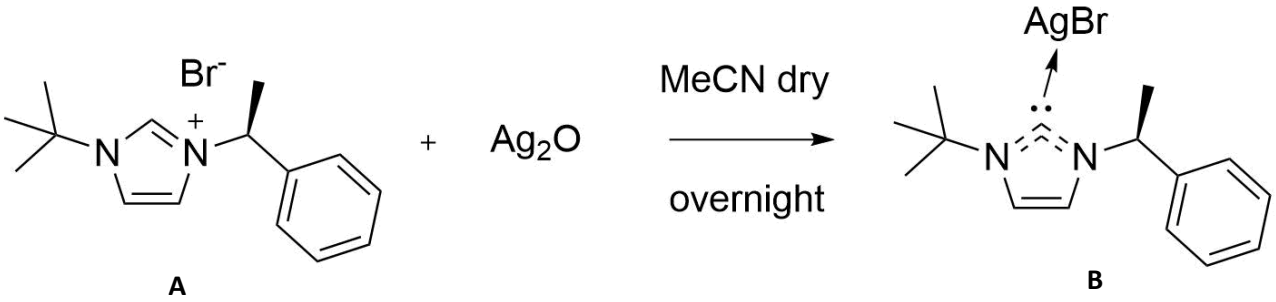

A **B**

A (0.201 g, 0.650 mmol, 1eq) was dissolved in dried MeCN (15 mL) in a flask. Then Ag_2O (1.95 mmol, 3 eq) was added. The flask was closed and covered with tinfoil. The reaction was left overnight. The product was filtered under vacuum and then dried with a rotary evaporator. It was very hydrophilic, so it was stored under vacuum until the reaction. The product was a pale yellow oil.

5- 4-methoxybenzenediazonium hexafluorophosphate

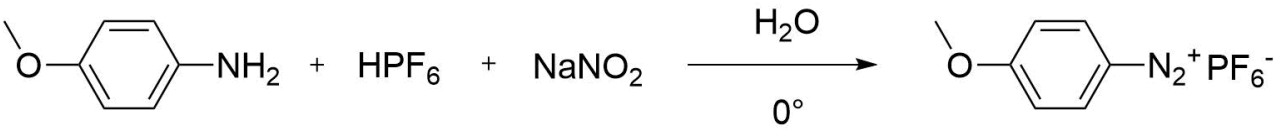

C

4-methoxyaniline (0.372 g, 3 mmol, 1 eq) was placed in a flask with water (100 mL). The flask was vigorously stirred in an ice bath. Hexafluorophosphoric acid (60% 1.34 mL, 8.1 mmol, 2.7 eq) was added dropwise to the flask until all the solid was dissolved. $NaNO_2$ (0.310 g, 4.5 mmol, 1.5 eq) was dissolved in water and then poured dropwise into the solution. The formation of a white solid was immediately observed. It was left to react for about an hour. The solid was filtered under vacuum and washed with ether. It appeared as a white powder.

6- Molecular motor E-2

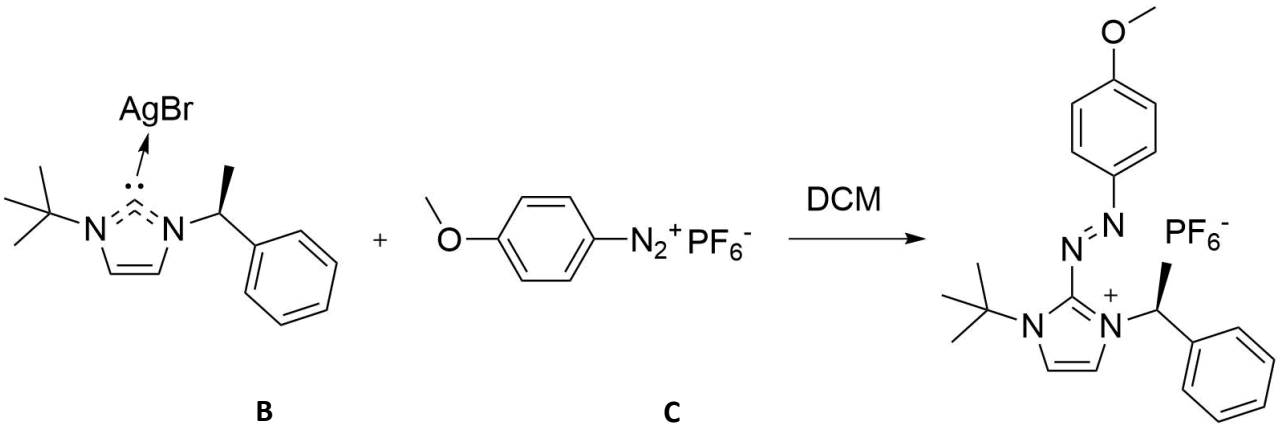

B **C** **E-2**

The silver salt **B** (0,240 g, 0,58 mmol, 1 eq) is dissolved in DCM (10 ml) and then the diazonium salt **C** (0,484 g, 1,74 mmol, 3 eq) was added. The flask was placed in agitation, cooled down in an ice bath. The solution was become intense orange and the formation of a white solid (AgBr) was immediately observed. The solid was filtered and the liquid dried with a rotary evaporator. Subsequently, the product is left with vacuum for few hours. To remove the starting material, the product was extracted with a separating funnel. NH_4PF_6 was dissolved in water. Three extractions were made. In this way, everything that wasn't PF_6 is passed into aqueous solution. Then the solution was washed with water. Finally, the clear dark orange solution was collected. Na_2SO_4 was added to dry. The solution was filtered and dried with a rotary evaporator. To purify the product, two GPCs were performed in DCM. The final product was obtained very clean. ^{1}H NMR (500 MHz, 298 K, Chloroform-*d*) δ 7.90 (d, **J = 9.05** Hz, 2H **14**), 7.71 (d, *J* = 2.3 Hz, 1H **4**), 7.60 (d, *J* = 2.3 Hz, 1H **5**), 7.36 (dd, J_1 = 7.05 Hz, J_2 = 1.7 Hz, 2H **9**), 7.30 (tt, J_1 = 7.30 Hz, J_2 = 2.05 Hz, 1H **11**), 7.20 (t, *J* = 6.95 Hz 2H **10**), 7.09 (d, ***J*= 9.2** Hz 2H **13**), 6.26 (q, *J* = 7.0 Hz, 1H **6**), 3.96 (s, 3H **16**), 1.91 (d, *J* = 7.0 Hz, 3H **7**), 1.81 (s, 10H **1**). ^{13}C NMR (126 MHz, 298 K, Chloroform-*d*) δ 166.66 (**15**), 147.25 (**12**), 143.88 (**3**), 138.65 (**8**), 129.34 (**9**), 128.86 (**11**), 127.31 (**14**), 126.30 (**10**), 120.86 (**4**), 119.77 (**5**), 115.63 (**13**), 63.89 (**2**), 60.14 (**6**), 56.25 (**16**), 30.13 (**1**), 21.63 (**7**).

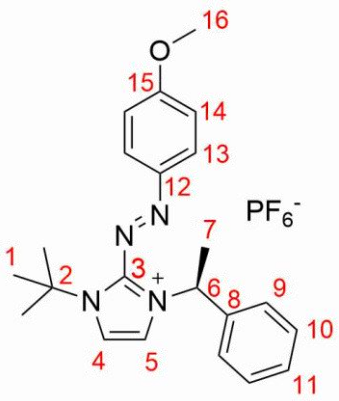

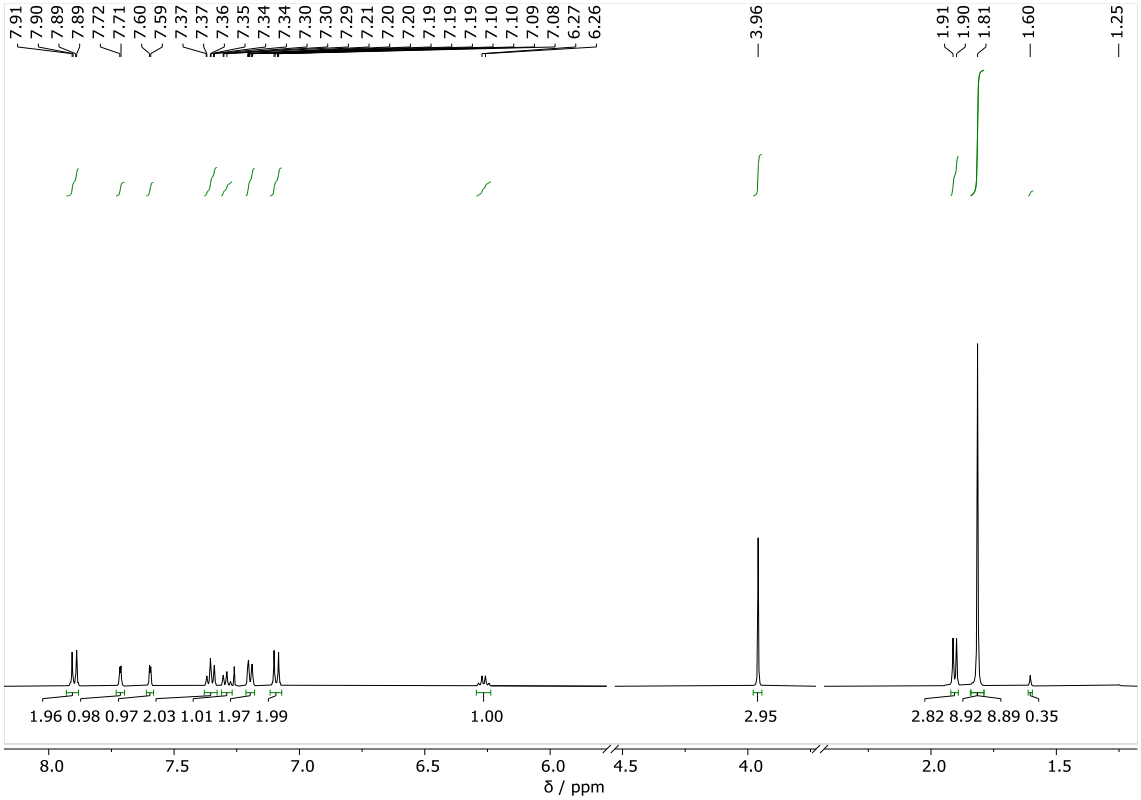

Figure 4.7. ^{1}H NMR spectrum of **E-2** (Chloroform-*d*, 298 K, 500 MHz)

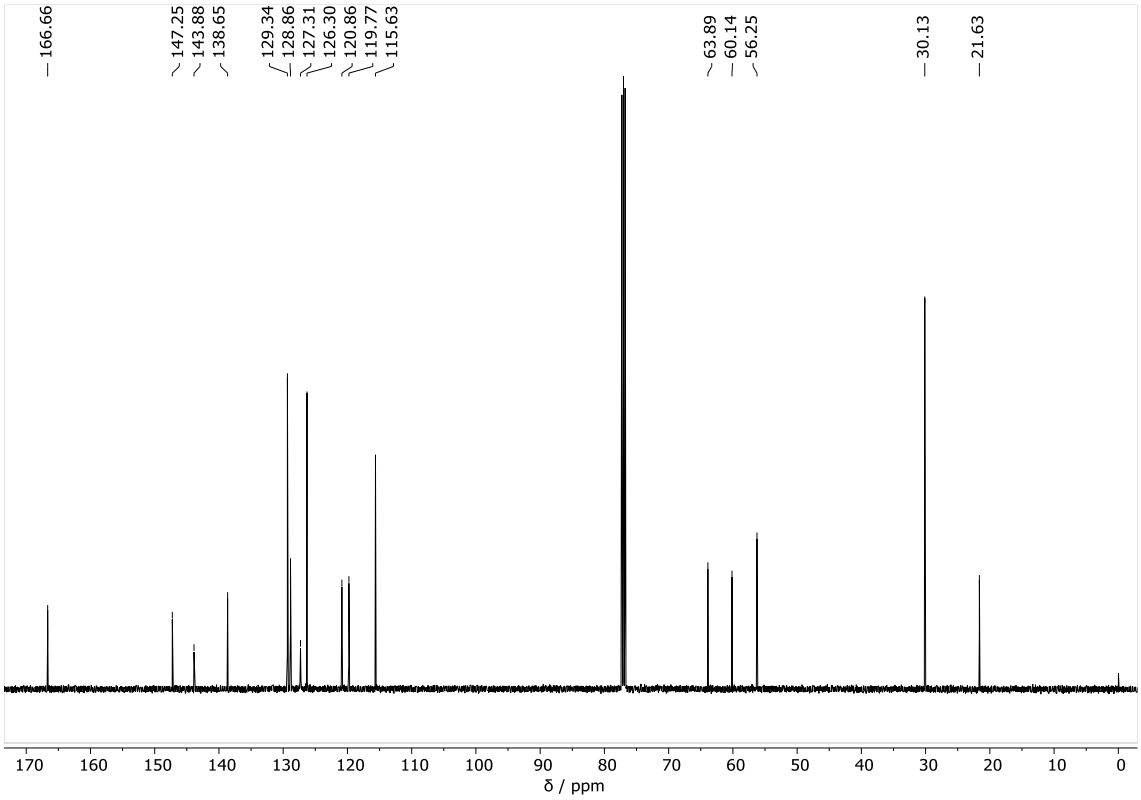

Figure 4.8. ^{13}C NMR spectrum of ***E*-2** (Chloroform-*d*, 298 K, 126 MHz)

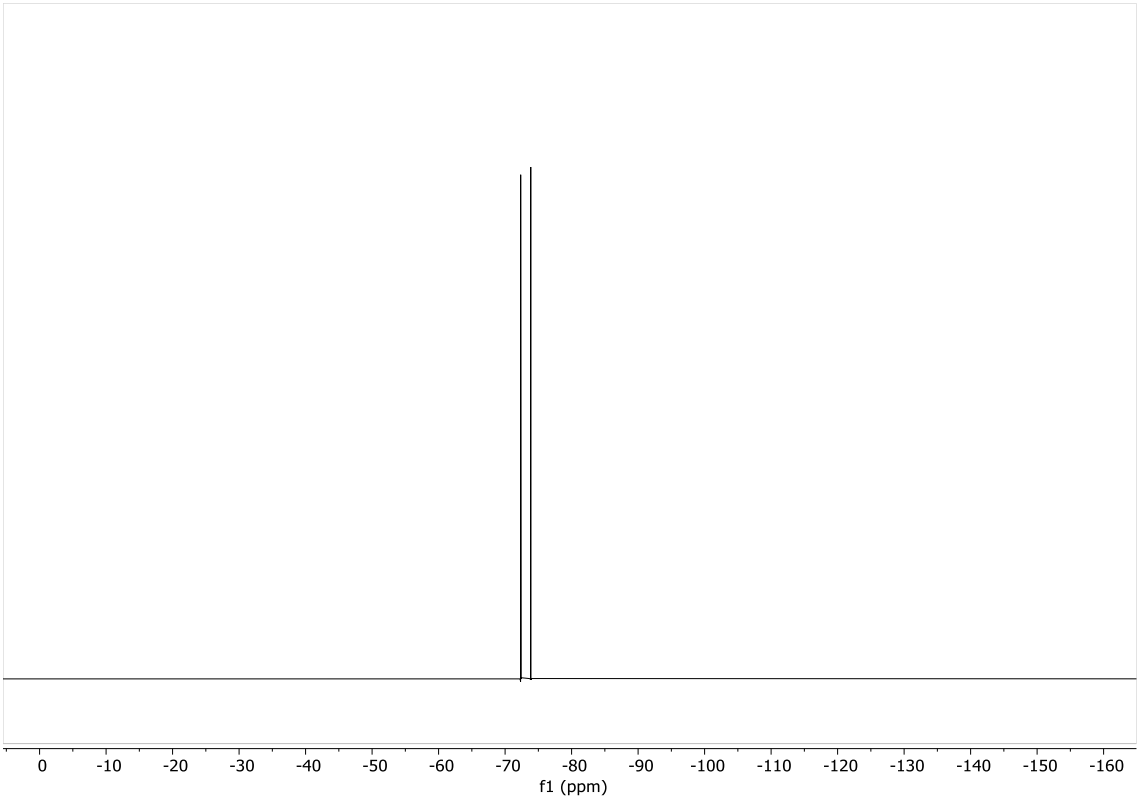

Figure 4.9. ^{19}F NMR spectrum of ***E*-2** (Chloroform-*d*, 298 K, 470 MHz)

7- 4-(tert-butyl)benzenediazonium hexafluorophosphate

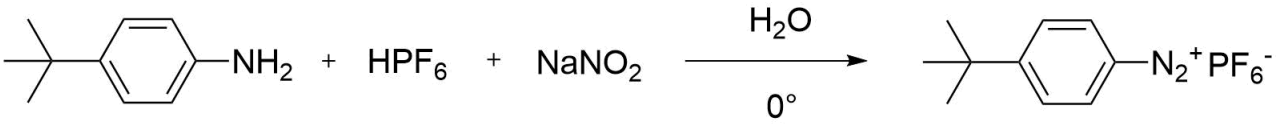

The 4-(tert-butyl)aniline (0,448 g, 3 mmol, 1eq) was placed in a flask with water (100 ml). The flask was vigorously stirred in an ice bath. Hexafluorophosphoric acid (60% 1,34 ml, 8,1 mmol, 2,7 eq) was added dropwise to the flask until all the solid was dissolved. $NaNO_2$ (0.310g, 4.5 mmol, 1.5 eq) was dissolved in water and then poured dropwise into the solution. The formation of a white solid was immediately observed. It was left to react for about an hour. The solid was filtered under vacuum and washed with ether. It appeared as a white powder.

8- Motor *E*-1

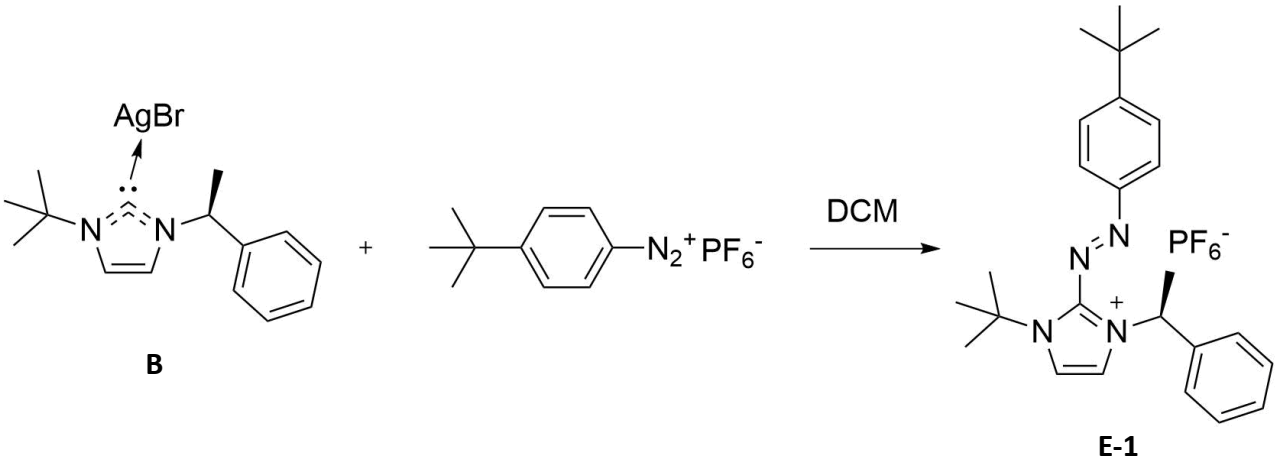

The silver salt **B** (0,240 g, 0,58 mmol, 1 eq) is dissolved in DCM (10 ml) and then the diazonium salt (0,876 g, 1,74 mmol, 3 eq) was added. The flask was placed in agitation, cooled down in an ice bath. The solution was become intense orange and the formation of a white solid (AgBr) was immediately observed. The solid was filtered and the liquid dried with a rotary evaporator. Subsequently, the product is left with vacuum for few hours. To remove the starting material, the product was extracted with a separating funnel. NH_4PF_6 was dissolved in water. Three extractions were made. In this way, everything that wasn't PF_6 is passed into aqueous solution. Then the solution was washed with water. Finally, the clear dark orange solution was collected. Na_2SO_4 was added to dry. The solution was filtered and dried with a rotary evaporator. To purify the product, two GPCs were performed in DCM. The final product was obtained very clean and appeared as orange solid. ^{1}H NMR (500 MHz, 298 K, Chloroform-*d*) 8.59 (d, ***J* = 2.40** Hz, 1H **4**), 8.39 (d, ***J* = 1.90 Hz**, 1H **5**), 7.78 (d , ***J* = 8.80 Hz** 2H **13**), 7.60 (d, ***J* = 8.95**, 2H **14**), 7.32 (dd, J_1= 9.45 Hz, J_2= 1.21 Hz, 2H **9**), 7.27 (m, 1H **11**), 7.22 (m, 2H **10**), 6.25 (q, ***J* = 7.10** Hz, 1H **6**), 1.97 (d, ***J* = 7.15 Hz**, 3H **7**), 1.83 (s, 9H **1**), 1.34 (s, 9H **17**). ^{13}C NMR (126 MHz, 298 K, Chloroform-*d*) δ 160.9 (**16**), 150.7 (**12**), 143.0 (**3**), 138.5 (**8**) , 129.4 (**9**) , 129.0 (**11**), 127.3 (**14**), 126.5 (**10**), 124.2 (**13**), 123.7 (**4**), 122.1 (**5**), 64.3 (**2**) , 60.5 (**6**), 35.8 (**15**), 31.0 (**17**), 30.6 (**1**) , 22.1 (**7**).

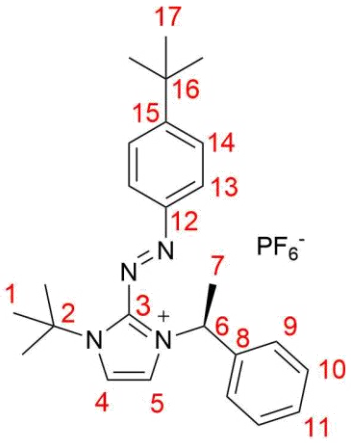

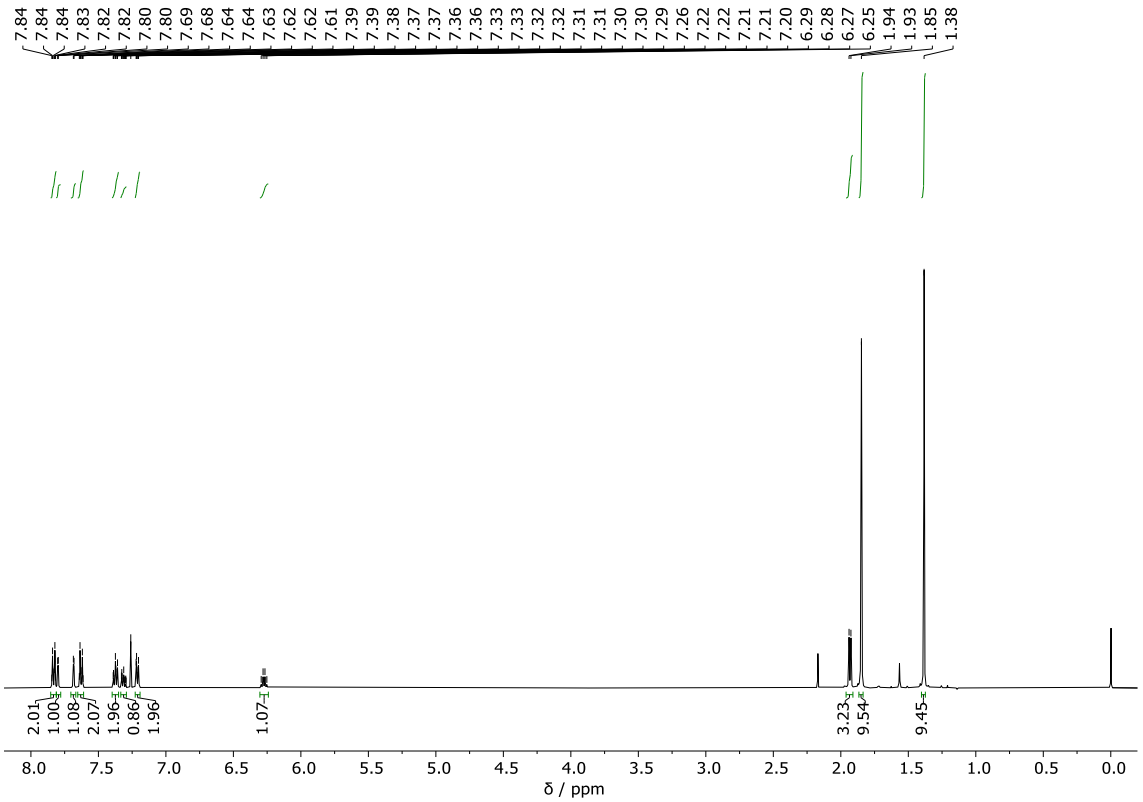

Figure 4.10. ^{1}H NMR spectrum of ***E*-1** (Chloroform-*d*, 298 K, 500 MHz)

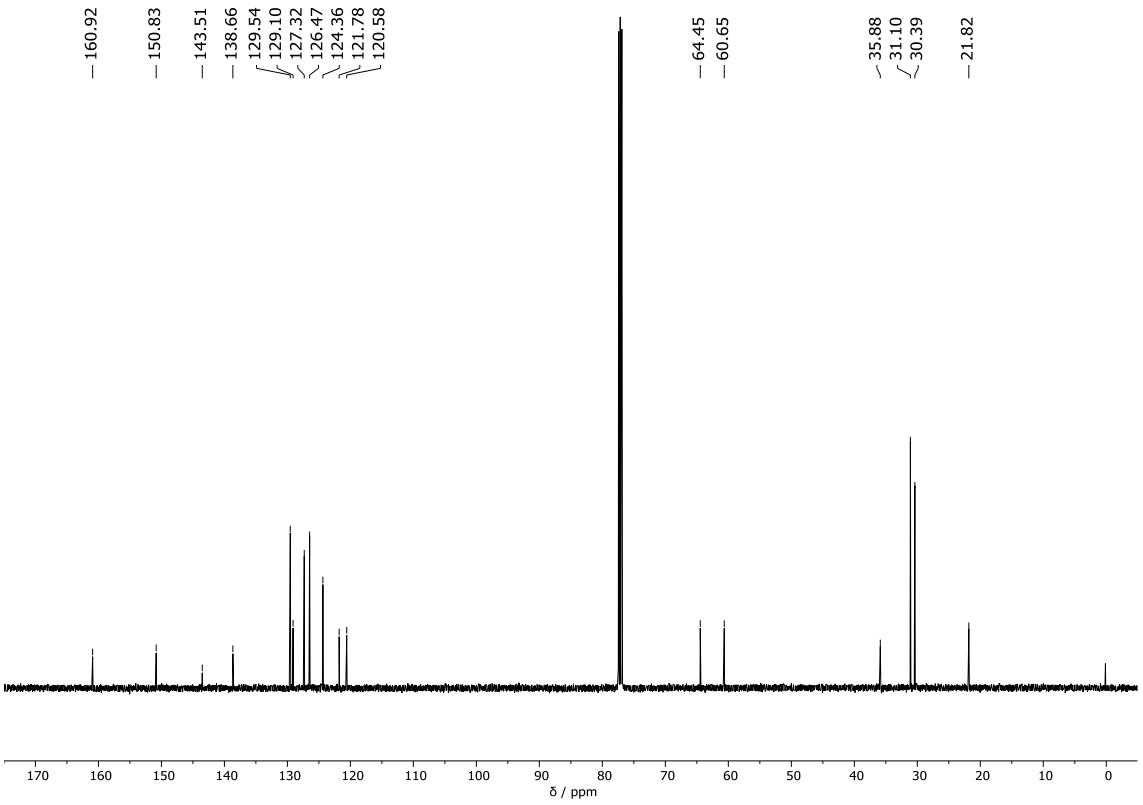

Figure 4.11. ^{13}C NMR spectrum of ***E*-1** (Chloroform-*d*, 298 K, 126 MHz)

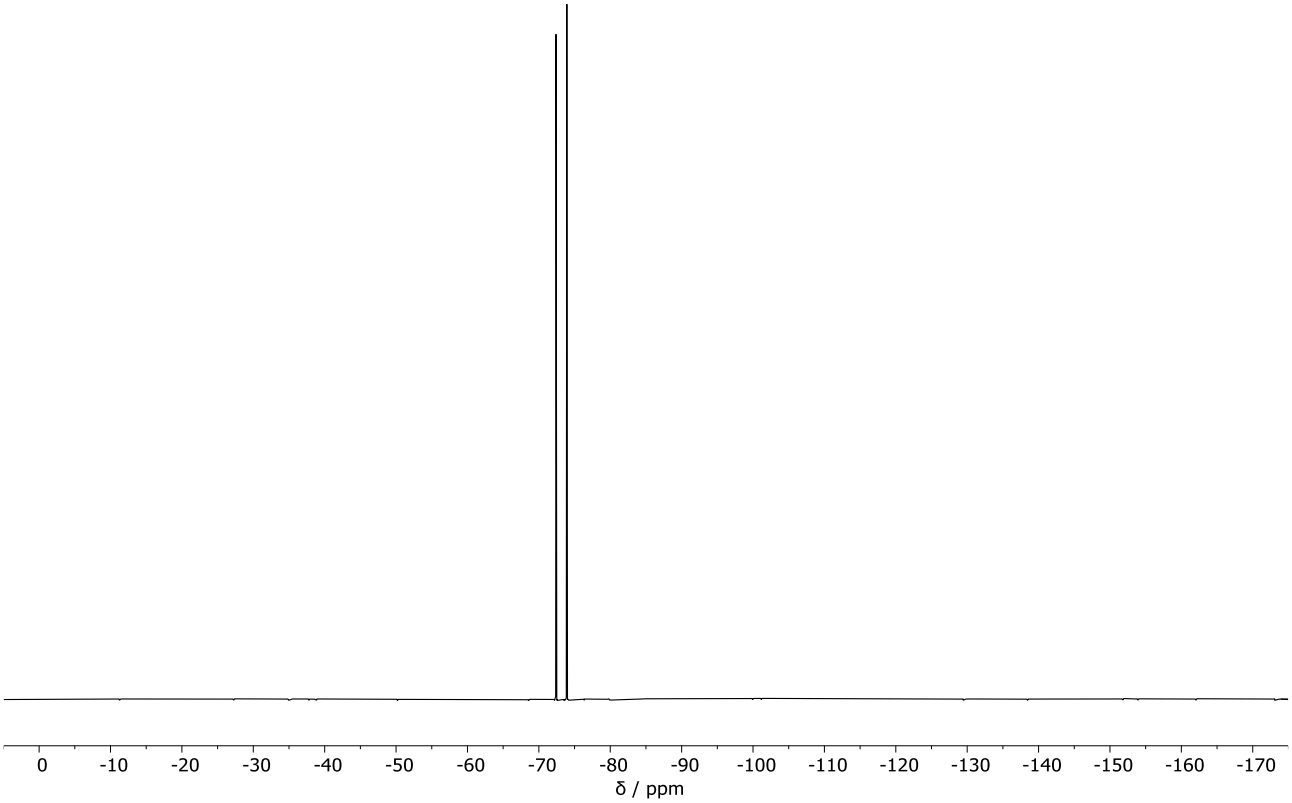

Figure 4.12. ^{19}F NMR spectrum of ***E*-1** (Chloroform-*d*, 298 K, 470 MHz)

9- Motor *E*-3

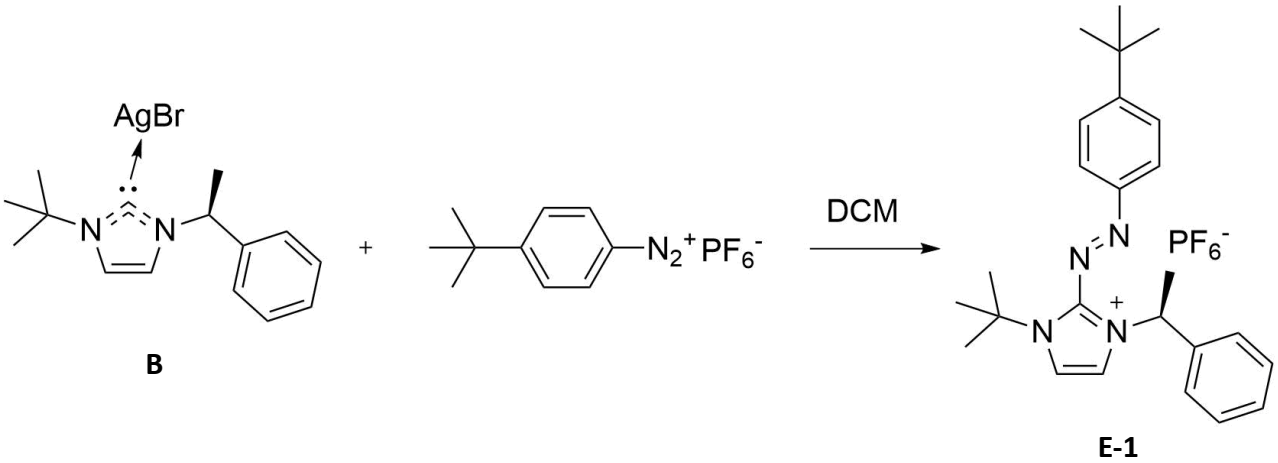

B **E-1**

The silver salt **B** (0,240 g, 0,58 mmol, 1 eq) is dissolved in DCM (10 ml) and then the diazonium salt (0,876 g, 1,74 mmol, 3 eq) was added. The flask was placed in agitation, cooled down in an ice bath. The solution was become intense orange and the formation of a white solid (AgBr) was immediately observed. The solid was filtered and the liquid dried with a rotary evaporator. Subsequently, the product is left with vacuum for few hours. To remove the starting material, the product was extracted with a separating funnel. NH_4PF_6 was dissolved in water. Three extractions

were made. In this way, everything that wasn't PF_6 is passed into aqueous solution. Then the solution was washed with water. Finally, the clear dark orange solution was collected. Na_2SO_4 was added to dry. The solution was filtered and dried with a rotary evaporator. To purify the product, two GPCs were performed in DCM. The final product was obtained very clean and appeared like an orange solid. Azoimidazolium chloride ***E*-3** was obtained through anion exchange of the corresponding hexafluorophosphate salt ***E*-1** upon repeated elution of a methanol solution over an ion exchange resin comprising polystyrene beads functionalised with tertiary ammonium chloride appendages. Yield: quantitative. ^{1}H NMR (500 MHz, 298 K, Chloroform-*d*) δ 8.59 (d, *J* = 2.30 Hz, 1H **4**), 8.39 (d, J= 1.9 Hz, 1H **5**), 7.80 (d, J = 8.8 Hz, 2H **13**), 7.60 (d, *J* = 8.95 Hz, 2H **14**), 7.32 (dd, J_1 = 7.15 Hz , J_2= 1.51 Hz, 2H **9**), 7.23 (m, 2H **10**), 6.25 (q, *J* = 7.10 Hz, 1H **6**), 1.97 (d, *J* = 7.10 Hz, 3H **7**), 1.85 (s, 9H **1**), 1.34 (s, 9H **17**). ^{13}C NMR (126 MHz, 298 K, Chloroform-*d*) δ 160.83 (**16**), 150.56 (**15**), 142.95 (**3**), 138.40 (**8**), 129.33 (**9**), 128.96(**11**), 127.21 (**14**), 126.42 (**10**), 124.09 (**13**), 123.61 (**5**), 122.02 (**4**), 64.24 (**2**) 60.42 (**6**), 35.72 (**12**), 30.92 (**17**), 30.52 (**1**), 21.98 (**7**).

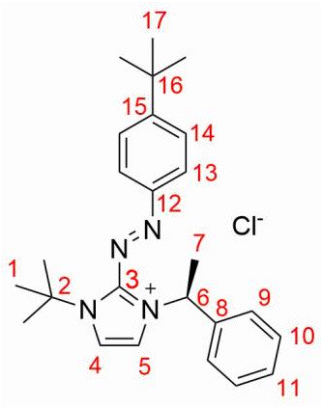

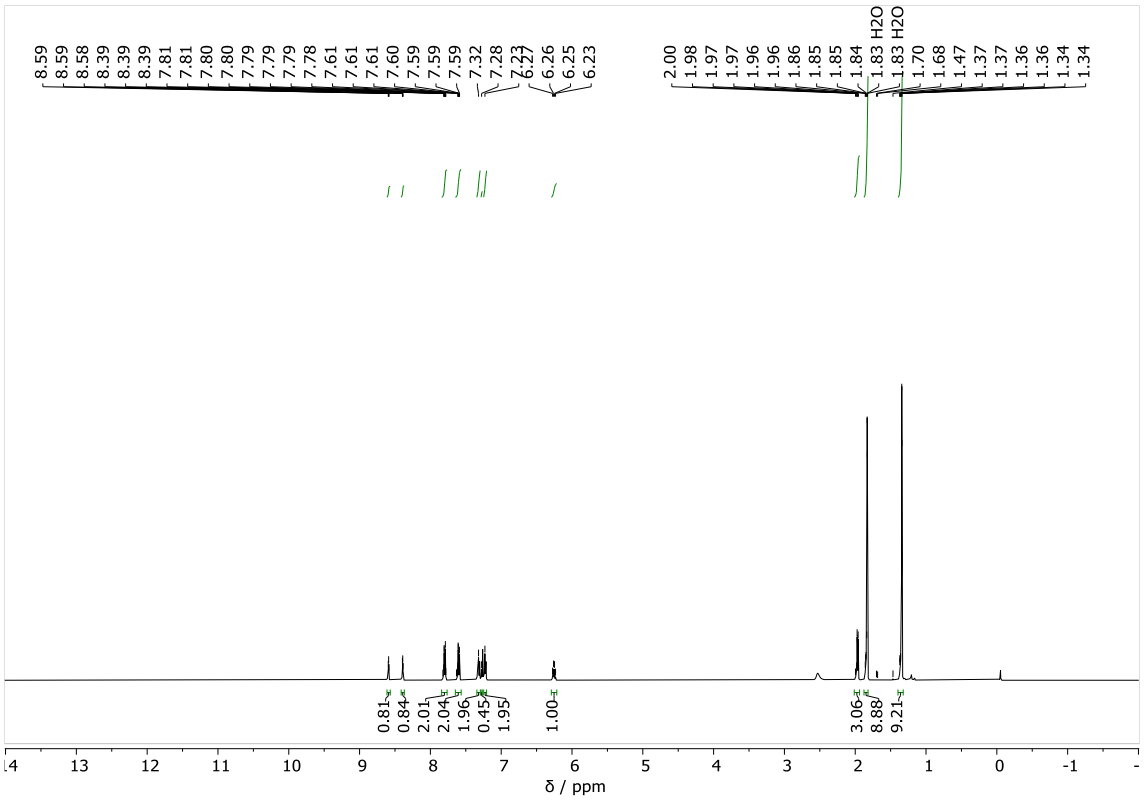

Figure 4.13. ^{1}H NMR spectrum of ***E*-3** (Chloroform-*d*, 298 K, 500 MHz)

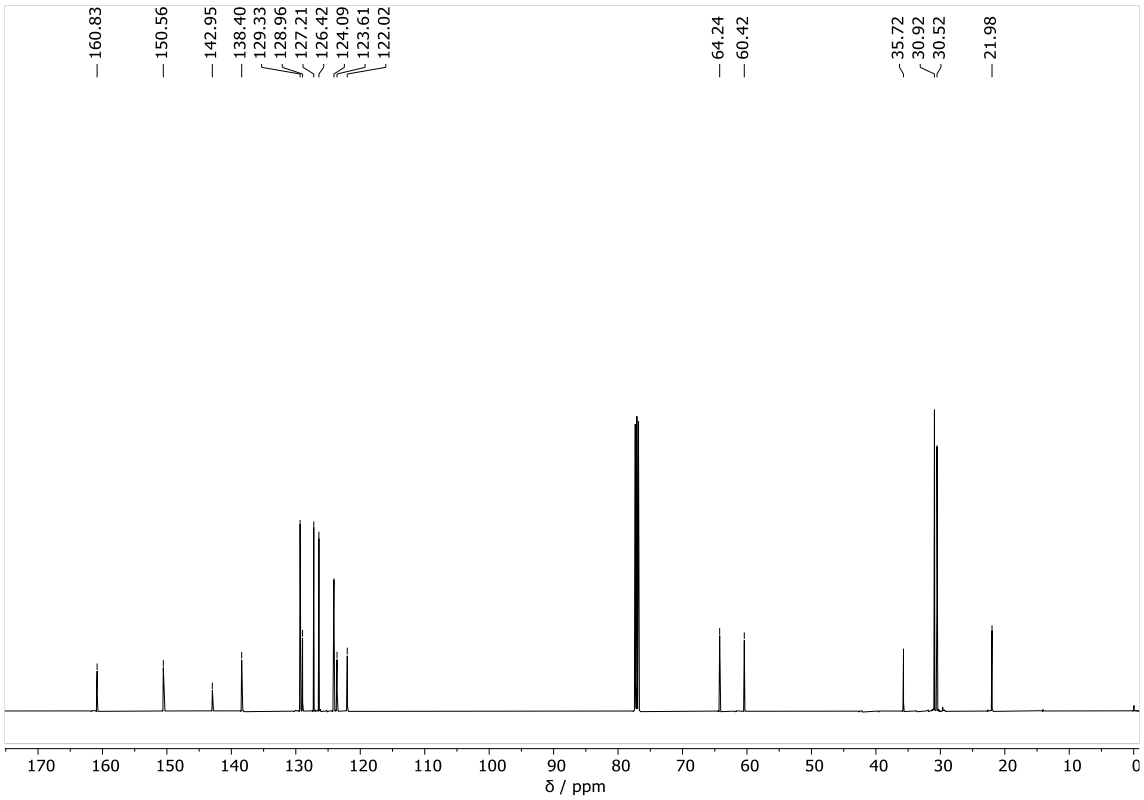

Figure 4.14. ^{13}C NMR spectrum of ***E*-3** (Chloroform-*d*, 298 K, 126 MHz)

REFERENCES:

1) Mondal, A.; Toyoda, R.; Costil, R.; Feringa, B. L. *Angew. Chem. Int. Ed.* **2022**, *61*, e20220663.
2) Corrà, S.; Curcio, M.; Credi, A. *JACS Au* **2023**, *3*, 1301-1313.
3) Roke, D.; Wezenberg, S. J.; Feringa, B. L. *Proc. Natl. Acad. Sci. U.S.A.* 2018, *115*, 9423-9431.
4) Baker, M. A. B.; Berry, R. M. *Contemp. Phys.* **2009**, *50*, 617-632.
5) Baroncini, M.; Silvi, S.; Credi, A. *Chem. Rev.* **2020**, *120*, 200-268.
6) Xue, R.; Ma, Q.; Baker, M. A.; Bai, F. A Delicate Nanoscale Motor Made by Nature—The Bacterial Flagellar Motor.
7) Bandara, H. M. D.; Burdette, S. C. *Chem. Soc. Rev.* **2012**, *41*, 1809-1825.
8) Kassem, S.; van Leeuwen, T.; Lubbe, A. S.; Wilson, M. R.; Feringa, B. L.; Leigh, D. A. *Chem. Soc. Rev.* **2017**, *46*, 2592.
9) Zhang, L.; Qiu, Y.; Liu, W.-G.; Chen, H.; Shen, D.; Song, B.; Cai, K.; Wu, H.; Jiao, Y.; Feng, Y.; Seale, J. S. W.; Pezzato, C.; Tian, J.; Tan, Y.; Chen, X.-Y.; Guo, Q.-H.; Stern, C. L.; Philp, D.; Astumian, R. D.; Goddard, W. A., III; Stoddart, J. F. An Electric Molecular Motor. *Nature* **2023**, *613*, 280-286.
10) Li, Q.; Fuks, G.; Moulin, E.; Maaloum, M.; Rawiso, M.; Kulic, I.; Foy, J. T.; Giuseppone, N. *Nat. Nanotechnol.* **2015**, *10*, 161-165.
11) Astumian, R. D. *Nat*. *Nanotechnol.* **2012**, *7*, 684-688.
12) Ragazzon, G.; Baroncini, M.; Silvi, S.; Venturi, M.; Credi, A. *Nat*. *Nanotechnol.* **2015**, *10*, 70-75.
13) Fuchter, M. J. *J. Med. Chem*. **2020**, *63*, 11436-11447.
14) Balzani, V.; Credi, A. *Le macchine molecolari* (Edizione 1088press, 2018)
15) Nicoli, F.; Taticchi, C.; Lorini, E.; Borghi, S.; Aleotti, F.; Silvi, S.; Credi, A.; Garavelli, M.; Muccioli, L.; Baroncini, M.; Curcio, M. *ChemRxiv* **2024**; DOI: 10.26434/chemrxiv-2024-03sk0.
16) Yoshida, M.; Muneyuki, E.; Hisabori, T. *Nat. Rev. Mol. Cell. Biol.* **2001**, *2*, 669-677.
17) Hüll, K.; Morstein, J.; Trauner, D. *Chem. Rev.* **2018**, *118*, 10710-10747.
18) Casimiro, L.; Andreoni, L.; Groppi, J.; Credi, A.; Métivier, R.; Silvi, S. *Photochem. Photobiol. Sci.* **2022**, *21*, 825-833.
19) Gandolfi, M. T.; Juris, A.; Moggi, L. *Manuale del fotochimico, Tecniche e metodologie* (Bologna University Press, 2006).
20) Stranius, K.; Börjesson, K. *Sci. Rep.* **2017**, *7*, 41145.
21) Koumura, N.; Zijlstra, R. W. J.; van Delden, R. A.; Harada, N.; Feringa, B. L. *Nature* **1999**, *401*, 1997-2000.